

# Displacement memory in regular black hole spacetimes

Ritwik Acharyya\* and Sayan Kar†

Department of Physics, Indian Institute of Technology, Kharagpur 721 302, India

Displacement memory, induced by a wave pulse in a regular black hole spacetime, is studied using geodesic (timelike) separation and geodesic deviation. The presence of the wave pulse in such a black hole is modeled via a function  $H(u)$  appearing in a restricted version of a generic Bondi-Sachs type line element. Choosing a sech-squared profile for  $H(u)$ , we first study (numerically) geodesic separation and geodesic deviation in a flat background. Thereafter, similar investigations are carried out in the presence of the black hole, but in regions far away from the vicinity of the horizon. Our results suggest the presence of a distinct displacement memory effect, which depends on the value of the regularisation parameter  $g$  as well as the pulse height. Between different types of regular black holes, one notices parameter-dependent changes in the net displacement memory. Further, a clear difference in the magnitude of displacement memory (at large  $u$ ) in regular and singular black holes is also visible in our numerical results.

## I. INTRODUCTION AND SUMMARY

The detection of gravitational waves (GW) has significantly advanced gravitational physics over the past decade [1–3]. Besides detection, such observations also provide indirect proof of binary black hole (or binary neutron star [4], black hole-neutron star) merger events and the subsequent emergence of a perturbed black hole [5]. The behaviour of gravity in strong fields is, in a way, tested in these observations, which, in turn, test general relativity (GR) against other modified theories of gravity [6, 7]. In addition, questions on the nature of matter in compact objects characterised through their equations of state or the tidal response of a compact object [8–10] can be/are being addressed via such GW observations.

Another remarkable, but as yet undetected consequence in gravitational wave physics and interferometric detection is the possibility of detecting a new phenomenon known as gravitational wave memory [11–13]. GW memory is a theoretically known effect in General Relativity (GR) (or even in other gravity theories [14]). Till date, however, it has not been confirmed observationally in astrophysical data [15]. The concept was first proposed in the work by Zel'dovich and Polnarev [16] and developed further by Braginsky and Grishchuk [17]. A fully non-linear treatment of GW memory within general relativity was discussed by Christodoulou [18] and later extended by Thorne and others [19, 20]. It was shown that gravitational waves propagating to null infinity generate an additional, permanent displacement in the detector response. This contribution, arising from the non-linear structure of Einstein's equations, is now referred to as the *nonlinear (Christodoulou) memory*. More recent developments by Bieri and Garfinkle [21], using gauge-invariant observables, revealed that the earlier linear–nonlinear classification is somewhat misleading, since both contributions can, in principle, arise within the framework of linearized gravity. Consequently, there has been a reclassification as ordinary and null memory effects, corresponding respectively to gravitational radiation sourced by massive and massless particles [22].

Over the past few years, GW memory has been investigated in a wide range of theoretical and phenomenological contexts. It arises in different incarnations which include displacement memory [23–25], velocity memory [26, 27], spin memory [28, 29] and in electromagnetsim, as electromagnetic memory [30–32]. Allied studies have formulated memory in the broader framework of persistent observables [33, 34] and examined them in detail [35]. Extensions to post-Newtonian and self-force formalisms have provided further insight into its generation in compact binary systems [36], while analogous effects have been explored in pp-wave [37–39] and cosmological spacetimes [40, 41]. Memory effects appear as an element in the so-called infrared triangle, which connects memory, asymptotic symmetries, and soft theorems [42–44]. Various other studies have addressed the influence of astrophysical environments on memory [45, 46]. Numerical relativity simulations have confirmed that nonlinear memory grows significantly during the late inspiral and mergers [47], with its amplitude and detectability strongly influenced by the spin and mass ratios of the sources [48–50]. A comprehensive overview of theoretical and computational developments around GW memory may be found in [51].

\*Email address: [ritwikacharyya@kgpian.iitkgp.ac.in](mailto:ritwikacharyya@kgpian.iitkgp.ac.in)

†Email address: [sayan@phy.iitkgp.ac.in](mailto:sayan@phy.iitkgp.ac.in)

The essence of GW memory lies in a *permanent change caused by a pulse*. It is found that once a gravitational wave pulse arrives and leaves the detector, there is a lasting effective change in the interferometer arm-lengths through a change in the very definition of distance, caused by the pulse, in the vicinity of the detector. The magnitude of this change is a couple of orders smaller than the amplitudes observed in GW detection [52]. It may appear (theoretically) as a net d.c. effect [53] on the observed GW strain, which adds to the time domain profile of a perturbed geometry. Hence, initial and final geodesic separations will differ, leading to a measurable GW memory. Collectively, all the above-mentioned investigations project GW memory as a rapidly advancing area of research, providing deep insights into the symmetry structure of spacetime and offering promising prospects for future detection. The growing interest in gravitational wave (GW) memory is further driven by its potential observability with upcoming detectors such as Advanced LIGO and LISA [54–56]. Recent investigations have developed waveform models and data-analysis strategies aimed at identifying memory signatures in current and future observations [57–62]. The wide range of studies around GW memory highlights its increasing relevance in the broader context of gravitational wave astronomy.

One can study GW memory in various ways, as mentioned above and in various articles and reviews. Here, we consider the approach where a restricted Bondi-Sachs type line element [63] is assumed, with a pulse in it signaling the brief presence of a wave. We study geodesic separation and geodesic deviation in typical background spacetimes by including the presence of the pulse in the line element. In this way, we try to determine if there is a permanent change in future regions where the pulse is insignificant (almost absent), as an indicator of a memory effect. This theoretical framework provides a direct means to connect the underlying spacetime geometry with signatures of GW memory and to probe nonlinear aspects of GR [46]. Earlier work around this approach may be found in [64–66].

Though initially we work in a flat background in Eddington-Finkelstein coordinates, later, we consider regular black holes [67, 68] as backgrounds. Let us briefly recall the idea of regular black holes. It is well-known that spacetime singularities remain an unresolved challenge in physics (see, for example, [69] for an overview and [70] for some cosmological implications). However, given the strict uniqueness theorems associated with the vacuum Einstein–Maxwell equations, any nonsingular (regular) black hole must incorporate some form of exotic matter, additional fields, or a modified internal structure. The construction of such regular black holes has been a topic of active current research interest [71–74]. Such regular spacetimes address the singularity problem in GR in a classical way and attempts to create and exploit scenarios circumventing the assumptions of the singularity theorems (e.g., violation of the Strong Energy Condition [75]). The early work of Bardeen, followed by later papers by Hayward, Neves–Saa, and others, provides examples of regular black hole geometries which we use in our analysis. There are other recent studies [76, 77] where the parameters of the regular black holes are constrained using the Event Horizon Telescope (EHT) data. Signatures that distinguish regular black holes from the singular ones, offer an indirect test of alternative approaches to resolve the singularity problem in general relativity. Likewise, through our studies here of parameter dependencies on displacement memory, we intend to uncover how such physical effects in regular black hole spacetimes may differ from similar effects in singular black holes. Thus, in addition to demonstrating the presence of memory, we may also be able to recognize if the background spacetime has a singularity or is regular.

Throughout this work, we use natural units ( $c = 1$ ). Our article is organised as follows. In the next section, we first discuss regular black holes and thereafter introduce the restricted Bondi-Sachs line element used in our studies, in a generic way. We introduce a pulse in the geometry and write down the geodesic equations for the modified line element. A brief analysis of the matter required to support such a geometry with a pulse is then presented. In Section III, we briefly recall the memory effect and state our approaches in studying memory in the given context. Section IV contains the details of the numerical results on memory as obtained from our analysis. In Section V, we briefly present our results on geodesic deviation, while Section VI contains our conclusions.

## II. REGULAR BLACK HOLES WITHOUT AND WITH A PULSE

The line element for a generic static, spherically symmetric spacetime, in the Schwarzschild gauge may be written as

$$ds^2 = -f(r)dt^2 + \frac{dr^2}{f(r)} + r^2(d\theta^2 + \sin^2\theta d\phi^2) \quad (1)$$

where,

$$f(r) = 1 - \frac{2m(r)}{r} \quad (2)$$

The following choice of  $m(r)$  (as proposed in [78]),

$$m(r) = \frac{M_0}{(1 + (\frac{g}{r})^b)^{a/b}} \quad (3)$$

gives a parametrized family of regular black holes. Here  $g$  is the regularisation parameter, related to the central density of a de Sitter core, which replaces the central singularity, thereby yielding a regular spacetime. For  $a = 3$  and  $b = 2$ , we have the well-known Bardeen class [79] of regular black hole solutions, whereas, for  $a = 3$  and  $b = 3$ , we have the Hayward class [80]. Numerous other solutions may be written down by choosing values of the parameters  $a$  and  $b$ . We will use the above-mentioned  $f(r)$  ( $m(r)$ ) as well as other known forms of  $f(r)$  representing regular black holes, while analysing displacement memory.

Given a regular solution, we now need to include a pulse in the spacetime metric in order to study a memory effect. To this end, we switch to outgoing Eddington–Finkelstein (EF) coordinates  $(u, r, \theta, \phi)$ , since the  $u$  coordinate parametrizes outgoing null rays along which waves can propagate. We express the spacetime metric as the combination of the metric  $g_{\mu\nu}$ , which is given by (1), and an additional piece  $h_{\mu\nu}$ , which encodes the pulse through a chosen functional form. Therefore, in the EF coordinates, the new geometry with the pulse may be chosen as

$$ds^2 = -f(r)du^2 - 2dudr + (r^2 + rH(u))d\theta^2 + (r^2 - rH(u))\sin^2\theta d\phi^2 \quad (4)$$

where  $H(u)$  encodes the details of the pulse (characterized by  $H''(u)$ ). Note that the above specific form is a choice that we justify later. The function  $H(u)$  is further assumed as

$$H(u) = A \operatorname{sech}^2(w(u - u_0)) \quad (5)$$

which does represent a pulse (centre at  $u = u_0$ ) where  $A$  and  $w$  are its amplitude and width, respectively. Later, while writing down the geodesic deviation equation in such a geometry, we shall see that the Riemann tensor contributes terms on its R.H.S. which are proportional to  $H''(u)$ . Such terms act as a forcing [17] over a finite interval (e.g., pulse) of the retarded time  $u$ . As we will see, this pulse induces a permanent displacement of test particles, thereby giving rise to the displacement memory effect.

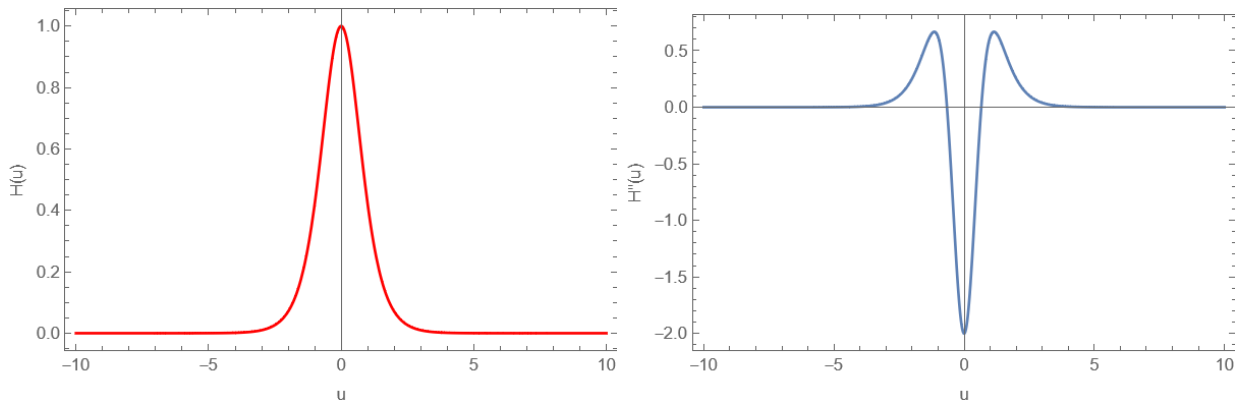


Figure 1: Pulse profile ( $H(u)$ ) with the parameters  $A = 1$ ,  $u_0 = 0$ ,  $w = 1$  and its double derivative.

We now attempt to interpret the nature of the metric in terms of the Bondi–Sachs framework. In 1960, Bondi introduced a novel approach [81] to study gravitational waves within Einstein’s theory of general relativity, formulated on the basis of null rays along which the waves propagate. Shortly thereafter, Sachs extended this formalism to non-axisymmetric spacetimes [82], providing a systematic analysis of the asymptotic symmetries along outgoing null hypersurfaces approaching null infinity. The Bondi–Sachs formalism requires only six independent metric functions to fully characterize the asymptotic structure of a general spacetime. In this context, the line element given in Eq. (4) may be regarded as a restricted version of the generic Bondi–Sachs metric given by [63],

$$ds^2 = -Wdu^2 - 2e^{2\beta}dudr + r^2h_{ij}(dx^i - U^i du)(dx^j - U^j du) \quad (6)$$

where

$$h_{ij}dx^i dx^j = \frac{1}{2} (e^{2\gamma} + e^{2\delta}) d\theta^2 + 2\sinh(\gamma - \delta) \sin\theta d\theta d\phi + \frac{1}{2} (e^{-2\gamma} + e^{-2\delta}) \sin^2\theta d\phi^2. \quad (7)$$

Here,  $W$ ,  $\beta$ ,  $\gamma$ ,  $\delta$ ,  $U^i$  are functions of  $u$ ,  $r$  and angular coordinates  $x^j$ . From Eq. (6), we may obtain Eq. (4) with choices  $W = f(r)$ ,  $\beta = 0$ ,  $U^i = 0$  and  $2\gamma(u, r) = 2\delta(u, r) = rH(u)$ . It is easy to see that for  $\gamma$  small,  $e^{2\gamma} \sim 1 + 2\gamma$ ,  $e^{-2\gamma} \sim 1 - 2\gamma$  and Eq. (6) reduces to Eq. (4). Considered as a vacuum solution of the Einstein equations as  $r \rightarrow \infty$ , the Bondi-Sachs geometry represents the gravitational field due to an isolated, radiating source, at  $\mathcal{J}^+$  [63, 83]. In our work here, we will only deal with a short-duration pulse (through the function  $H(u)$ ), in a flat or a regular black hole background.

- In the flat background case  $f(r) = 1$  and the line element/metric in (4) can be treated as a perturbation on Minkowski spacetime, which satisfies the transverse-traceless (TT) gauge condition. Thus, the interpretation of a gravitational wave propagating on a Minkowski background holds.
- When the background is not flat, i.e.,  $f(r) \neq 1$ , however, the treatment of the deformation as a perturbation in the TT gauge is not quite valid – the Lorentz gauge condition is violated globally. Thus, a residual gauge freedom remains. The deformation can still be wave-like and gravitational, but it is not similar to the ‘perturbative’ sense in which we have a gravitational wave in the TT gauge in a flat background.
- A useful way to visualize this full geometry (including the pulse) is to consider a constant- $u$  hypersurface. In the absence of the pulse ( $H(u) = 0$ ), the angular part reduces to that of a round two-sphere of radius  $r$ . In contrast, whenever  $H(u)$  is nonzero, the angular sector is no longer spherical: the geometry of the  $u = \text{constant}$  slice is anisotropically deformed, resembling a squeezed or stretched sphere depending on the sign of  $H(u)$ . For small perturbations  $H(u) \ll r$ , the distortion is slight, while for comparable  $H(u)$  (w.r.t.  $r$ ), the surface departs strongly from spherical symmetry. This illustrates explicitly how the wave pulse induces a transient deviation from the two-sphere, which disappears once the pulse has passed. The relic of this deformation persists in the relative separation between geodesics as well as the deviation vector, and gives rise to the displacement memory effect, as we elucidate below.

To introduce this perturbation into our metric, we must incorporate an energy-momentum tensor in the matter sector which serves as the source for the pulse. Considering  $H/r$  to be very small, we can write the Einstein tensors up to the  $\mathcal{O}(\frac{H}{r})$  and we can check the effect of the presence of the pulse in the Einstein tensors compared to the vacuum case:

$$G_{uu} = \frac{r^4 f (1 - f - rf') - r^3 f H}{r^6} \quad G_{ur} = \frac{r^4 f (1 - f - rf') - r^3 H}{r^6} \quad (8)$$

$$G_{rr} = 0 \quad G_{u\theta} = \frac{\cot \theta H'}{r} \quad (9)$$

$$G_{r\theta} = -\frac{H \cot \theta}{r^2} \quad G_{\theta\theta} = \frac{4r^4 f' + 2r^5 f'' + 2r^3 H (2f' - rf'' - 3f')}{4r^3 (1 - \frac{H}{r})^2} \quad (10)$$

$$G_{\phi\phi} = \frac{\sin^2 \theta (4r^4 f' + 2r^5 f'' + H(2r^3 f' + 4r^4 f'' - 2r^4 f''))}{4r^3 (1 + \frac{H}{r})^2} \quad (11)$$

In the case of the Schwarzschild, where  $f(r) = 1 - 2m/r$ , we can write the Einstein tensors in the following way. The advantage of writing these tensors in this way is that we can see the effect of the pulse in the Einstein tensors more prominently up to the leading order of  $\mathcal{O}(\frac{H}{r})$ :

$$G_{uu} = \frac{-(1 - \frac{2m}{r}) H}{r^3} \quad G_{ur} = \frac{-H}{r^3} \quad G_{rr} = 0 \quad G_{u\theta} = \frac{\cot \theta H'}{r} \quad (12)$$

$$G_{r\theta} = \frac{H \cot \theta}{r^2} \quad G_{\theta\theta} = \frac{mH}{r^2} \quad G_{\phi\phi} = \frac{-mH \sin^2 \theta}{r^2} \quad (13)$$

The Einstein equations can equivalently be verified by decomposing the metric (4) as

$$g_{\mu\nu} = \hat{g}_{\mu\nu} + h_{\mu\nu}$$

where  $\hat{g}_{\mu\nu}$  denotes the background metric and  $h_{\mu\nu}$  represents a small perturbation characterized by  $H(u)$ . Expanding the Einstein tensor to linear order in the perturbation amplitude yields

$$G_{\mu\nu} = \hat{G}_{\mu\nu} + \delta G_{\mu\nu}$$

with  $\hat{G}_{\mu\nu}$  defined on the background spacetime and  $\delta G_{\mu\nu}$  denoting the first-order correction  $\mathcal{O}(H/r)$ . For a vacuum background with  $\hat{G}_{\mu\nu} = 0$ , the linear correction  $\delta G_{\mu\nu}$  can be computed explicitly, yielding Eqs. (12) and (13). This

allows a consistent verification of the matter sector in the perturbed spacetime. We note that for the Schwarzschild metric with no pulse ( $H(u) = 0$ ), the Ricci Tensors, Ricci Scalar, and Einstein tensors identically vanish, which is expected for a vacuum solution.

### III. OUR APPROACH IN STUDYING MEMORY EFFECTS

The gravitational wave memory effect has been studied in various ways in the literature. Among them are studies on the change in (a) geodesic separation [39, 65, 66] of two nearby geodesics in the distant future as compared to chosen values in the past and (b) geodesic deviation analysis [16]. The steps are outlined below.

- To study the burst-like nature of gravitational radiation, we have chosen a specific profile given by Eq. (5). The pulse is a function of the null coordinate  $u$ , which naturally characterizes the outgoing radiation. Such a choice is standard in studies of the gravitational-wave memory effect, as the net displacement memory is quantified by comparing the asymptotic behavior of geodesics at large  $u$ .
- The spacetime geometry is given by Eq. (4). We integrate the geodesic equations to obtain the timelike geodesics parametrised by  $u$ . Analytical or numerical methods may be used to solve for the spatial coordinates as functions of  $u$ . In this work, we numerically solved the geodesics with the proper choice of initial conditions.
- We have investigated the evolution of geodesic separation both in the presence and in the absence of a gravitational-wave pulse. The separation values before and after the passage of the pulse were compared. The resulting difference quantifies the *displacement memory effect*. Once the pulse has passed, the geodesic separation does not return to its initial value. Using the same choice of parameters and numerically integrated geodesics, we further studied the geodesic deviation.
- By differentiating the geodesic solutions and studying the evolution of their relative velocity, one can obtain a *velocity memory effect*. In the context of pp-wave backgrounds, pulse profiles satisfying  $\int_{-\infty}^{\infty} A(u)du \neq 0$  (where  $A(u)$  is the function representing the pulse in the pp-wave geometry) show a nonzero velocity memory [39, 84].

It is useful to note that while solving geodesics and finding geodesic separation, we are not making any assumption regarding the geodesics being ‘neighboring’, i.e., close to each other. On the other hand, while finding the deviation using the geodesic deviation equation, the equations themselves depend on the ‘neighboring geodesic’ assumption. Further, the deviation equations form a set of linear, second-order, coupled ordinary differential equations, whereas the geodesic equations are always quasi-linear.

In the next two sections, we will demonstrate our results for displacement memory using analysis of geodesic separation and geodesic deviation.

### IV. GEODESIC SEPARATION AND DISPLACEMENT MEMORY

Let us first write down the geodesic equations in the spacetime geometry given by Eq. (4). The effective Lagrangian can be written as,

$$L = -f(r)\dot{u}^2 - 2\dot{u}\dot{r} + (r^2 + rH(u))\dot{\theta}^2 + (r^2 - rH(u))\dot{\phi}^2 \quad (14)$$

Hence, the geodesic equations are,

$$\ddot{u} - \frac{f'}{2}\dot{u}^2 + \left(\frac{2r + H}{2}\right)\dot{\theta}^2 + \left(\frac{2r - H}{2}\right)\sin^2\theta\dot{\phi}^2 = 0 \quad (15)$$

$$2\ddot{r} + ff'\dot{u}^2 + 2f'\dot{r}\dot{u} + (rH' - f(2r + H))\dot{\theta}^2 + (-rH' - f(2r - H))\sin^2\theta\dot{\phi}^2 = 0 \quad (16)$$

$$\ddot{\theta}(r^2 + rH) + \dot{r}\dot{\theta}(2r + H) + \dot{\theta}\dot{u}rH' - \sin\theta\cos\theta(r^2 - rH)\dot{\phi}^2 = 0 \quad (17)$$

$$\ddot{\phi}\sin^2\theta(r^2 - rH) + 2\dot{\theta}\dot{\phi}\sin\theta\cos\theta(r^2 - rH) + \dot{\phi}\dot{r}\sin^2\theta(2r - H) - rH'\sin^2\theta\dot{\phi}\dot{u} = 0 \quad (18)$$

It can be checked that  $\theta = \pi/2$  is a solution of the above set of geodesic equations. An overdot denotes the derivative with respect to the proper time ( $\tau$ ),  $f'$  is  $df(r)/dr$ , and  $H'$  is  $dH(u)/du$ .

With  $\theta = \frac{\pi}{2}$ , the geodesic equations reduce to,

$$\ddot{u} - \frac{f'(r)}{2} \dot{u}^2 - \left( \frac{H(u) - 2r}{2} \right) \dot{\phi}^2 = 0 \quad (19)$$

$$\ddot{r} + \frac{f(r)}{2} f'(r) \dot{u}^2 + f'(r) \dot{r} \dot{u} + \frac{f(r)H(u) - 2f(r)r - rH'(u)}{2} \dot{\phi}^2 = 0 \quad (20)$$

$$\ddot{\phi} - \frac{H'(u)}{(r - H(u))} \dot{\phi} \dot{u} + \frac{2r - H(u)}{r^2 - rH(u)} \dot{\phi} \dot{r} = 0 \quad (21)$$

We are looking for timelike geodesics that must satisfy the timelike condition:

$$-f(r)\dot{u}^2 - 2\dot{u}\dot{r} + (r^2 - rH)\dot{\phi}^2 = -1 \quad (22)$$

The  $\phi$  equation yields a first integral

$$\dot{\phi} = \frac{L_c}{r^2 - rH}, \quad (23)$$

where  $L_c$  is the conserved angular momentum corresponding to the  $\phi$  coordinate. One can rewrite the above set of equations as a first-order dynamical system using the  $u$  coordinate as an independent variable (note that the pulse is a function of  $u$ ). We rewrite the timelike condition in the following way using Eq. (23):

$$-f(r)\dot{u}^2 - 2\dot{u}^2 \frac{dr}{du} + \frac{L_c^2}{r^2 - rH} = -1 \quad \Rightarrow \quad \dot{u}^2 = \frac{1 + \frac{L_c^2}{r^2 - rH}}{f(r) + 2\frac{dr}{du}} \quad (24)$$

Similarly,  $\ddot{r}$  and  $\ddot{\phi}$  can be written as

$$\ddot{r} = \frac{d^2r}{du^2} \dot{u}^2 + \frac{dr}{du} \dot{u} \frac{d}{du}(\dot{u}) \quad \ddot{\phi} = \frac{d^2\phi}{du^2} \dot{u}^2 + \frac{d\phi}{du} \dot{u} \frac{d}{du}(\dot{u}) \quad (25)$$

From (19) we can write:

$$\ddot{u} = \dot{u} \frac{d}{du}(\dot{u}) = \frac{f'(r)}{2} \dot{u}^2 + \left( \frac{H(u) - 2r}{2} \right) \dot{\phi}^2 \quad (26)$$

Hence using (23), and substituting the expressions for quantities like,  $\dot{u}^2$  and  $\dot{u} \frac{d}{du}(\dot{u})$  from (24) and (26) respectively, we can write the system of equations in  $u$  coordinate,

$$\frac{dp}{du} = -\frac{ff'}{2} [3p + f] - \frac{L_c^2}{(r^2 - rH)^2} \frac{f(r) + 2p}{1 + \frac{L_c^2}{r^2 - rH}} \left[ p \frac{H - 2r}{2} + \frac{fH - 2rf - rH'}{2} \right] \quad (27)$$

$$\frac{dq}{du} = -q \left[ \frac{f'}{2} - \frac{H'}{r - H} \right] - \frac{2r - H}{r^2 - rH} pq - q \frac{H - 2r}{2} \frac{L_c^2}{(r^2 - rH)^2} \frac{f(r) + 2p}{1 + \frac{L_c^2}{r^2 - rH}} \quad (28)$$

$$\frac{dr}{du} = p \quad (29)$$

$$\frac{d\phi}{du} = q \quad (30)$$

One can thus find  $p(u)$ ,  $q(u)$ ,  $r(u)$  and  $\phi(u)$  by numerical integration of the dynamical system. While solving, the timelike constraint has been added as a constraint on the variables in the dynamical system. Also, we have made careful choices of the initial conditions so that they satisfy the timelike condition throughout the evolution. Furthermore, to guarantee that the geodesics remain outside the event horizon, the initial radial coordinate  $r$  is chosen to lie beyond the horizon, with  $\dot{r}$  set positive through an appropriate choice of initial conditions. Velocity memory arises from (27), since for a pulse  $dH/du$  is different in the asymptotic limits  $u \rightarrow -\infty$  and  $u \rightarrow \infty$ . From the above set of equations, it is important to note that the occurrence of the gravitational wave memory effect requires a non-zero  $L_c$ . This is because  $H'(u)$  enters the equations multiplied by  $L_c$ , and the asymptotic change in  $H'$  is precisely what gives rise to the memory effect. Such a memory will also be visible if one plots the  $p(u)$  and  $q(u)$  as a vector field in two dimensions at large positive and negative values of  $u$ .

We will now numerically solve Eqs (27)–(30) and analyze various geometries, starting with the flat background.

### A. Flat background

For a flat background we have  $f(r) = 1$  in (4). Using the pulse profile from Eq. (5), we solve for geodesics and obtain the components of the geodesics  $r(u)$ ,  $\phi(u)$ . The chosen parameters for the pulse profile are:  $A = 3$  and  $w = 1$ . Thereafter, we investigate the separation of two nearby geodesics in the presence of the pulse and when it is absent. Numerical solutions of the geodesics are shown in Fig. (2). From the Fig. (2), it is evident that the geodesics

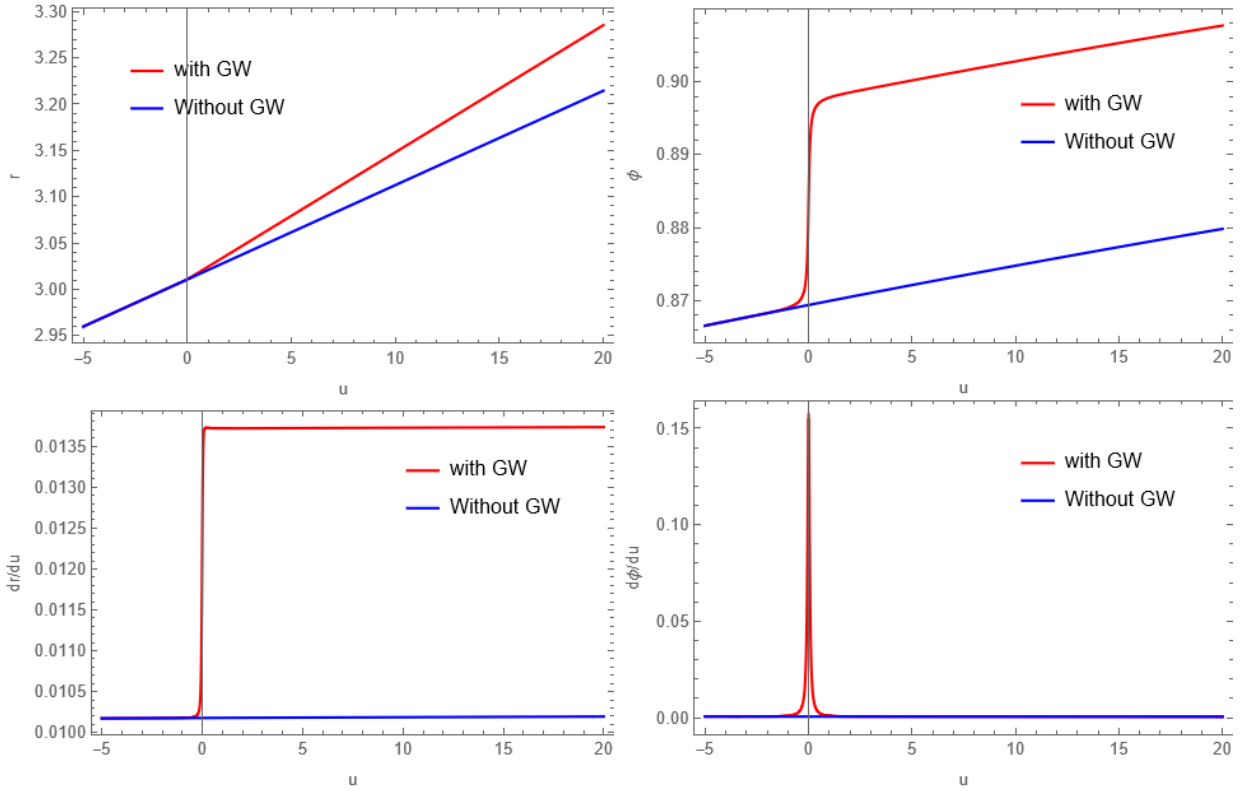


Figure. 2: **Top panel:** Geodesic components  $r(u)$  and  $\phi(u)$  with and without the GW pulse in flat spacetime. **Bottom panel:**  $dr/du$  and  $d\phi/du$  as functions of  $u$ , both in the presence and absence of GW pulse for flat metric. The values of the parameters are:  $L_c = 0.005$ , and  $A = 3$ .

evolve differently with respect to  $u$  in the presence and absence of the GW pulse. We next calculate the geodesic separations and plot their evolution as a function of  $u$ . As evident from Eq. (5), the pulse is significant around  $u = 0$  and subsequently decays rapidly. Below, we state the initial conditions used by us while solving the geodesic equations. Large positive and negative  $u$  values correspond to the choices  $u = 100$  units and  $u = -100$  units, respectively. The coordinates  $r(u)$  and  $\phi(u)$  are expressed in arbitrary units.

- Geodesic 1:  $r[-100] = 2$ ,  $p[-100] = 0.01$ ,  $\phi[-100] = \pi/4$ .
- Geodesic 2:  $r[-100] = 4$ ,  $p[-100] = 0.01$ ,  $\phi[-100] = \pi/4$ . The choice of  $q[-100]$  for both the geodesics has been discussed below.
- Given the initial condition on  $r$  and  $p$ , we use them in Eq. (24) to find  $\dot{u}$  at  $u = -100$ . We choose the positive root of  $\dot{u}$ . Thereafter, we set the initial condition for  $d\phi/du$  using the positive root of  $\dot{u}$  and Eq. (23).
- The parameter  $L_c$  is chosen to be small, since for  $L_c \gtrsim 0.005$  the separations in both  $r$  and  $\phi$  become negative at large  $u$ , indicating a crossing of geodesics. We therefore restrict our choice of  $L_c$  values appropriately.

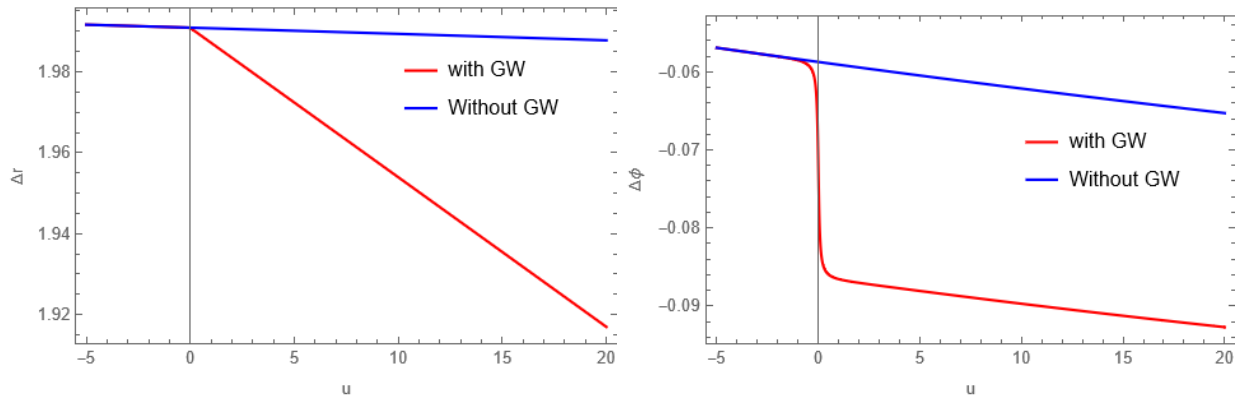


Figure 3: Variation of  $\Delta r$  and  $\Delta\phi$  with  $u$  for the flat metric, shown both in the presence and absence of a GW pulse. The chosen parameters are  $L_c = 0.005$  and  $A = 3$ .

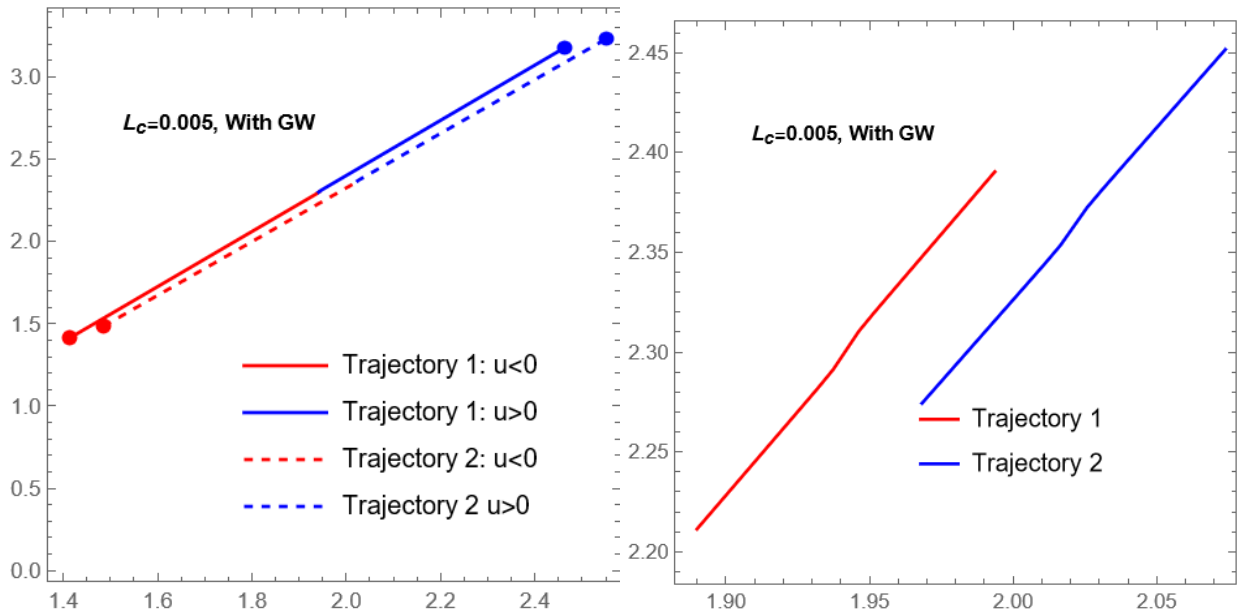


Figure 4: **Left panel:** Trajectories of two geodesics have been shown in the presence of the GW with  $L_c = 0.005$  and  $A = 1.5$ . The red dot represents  $u = -100$  and the blue dot marks  $u = +100$ . **Right panel:** Trajectories of the same pair of test particles shown in the region close to the GW pulse:  $u \in [-10, 10]$ .

In Figure (2) we have shown  $r$ ,  $\phi$ , and their  $u$  derivatives. Figure (3) shows the differences  $\Delta r$  and  $\Delta\phi$ . More precisely, we highlight the following key points.

- The differences in the coordinates are defined as

$$\Delta r = r(\text{geodesic 2}) - r(\text{geodesic 1}) \quad \Delta\phi = \phi(\text{geodesic 2}) - \phi(\text{geodesic 1}) \quad (31)$$

The geodesic separations evolve differently in the presence and absence of the wave pulse, and a residual difference persists at null infinity (which is different from the scenario with no pulse), indicating a displacement memory effect. However, the magnitude of the separation of two geodesics is very small at large  $u$ .

- In a flat background,  $\phi$  seems to be more sensitive to the GW pulse compared to  $r$ . In Fig. (3), this difference is clearly visible.

The picture becomes clearer if we plot the trajectories ( $r(\phi)$ ) of two geodesics and examine their asymptotic differences. Fig. (4) shows the two trajectories in the interval  $u \in [-100, 100]$ , with the red colour indicating  $u < 0$  and blue indicating  $u > 0$ . The point marked in red represents the starting point  $u = -100$  and the blue point represents the

end point  $u = +100$ . Having obtained  $r(u)$  and  $\phi(u)$ , the trajectories are plotted using  $x = r \cos \phi$  and  $y = r \sin \phi$ . For Fig. (4), we adopt the same set of boundary conditions as before, except that  $r[-100]$  is chosen to be 2 and 2.1 for the two geodesics, respectively. The intersection of the red and blue trajectories marks the  $u = 0$  region, where the effect of the gravitational wave pulse is maximum. The right panel provides a zoomed-in view near the pulse, illustrating the nature of the transition in both trajectories around  $u = 0$ . From the left panel of the Fig. (4), it is evident that the difference in trajectories between the two particles is smaller during the  $u < 0$  phase (red) compared to the  $u > 0$  phase (blue). This indicates that the GW pulse leaves an imprint on the relative trajectories, which remains even after the pulse has passed.

In the following subsections, we will carry out similar analyses for geodesics in various regular black holes, with the aim of establishing displacement memory as a signature capable of distinguishing between them as well as the related singular spacetime.

### B. Analysis for Bardeen spacetime

Let us begin by stating the  $f(r)$  for the Bardeen spacetime. We have,

$$f(r) = 1 - \frac{2}{r} \left[ \frac{M}{\left(1 + \left(\frac{g}{r}\right)^2\right)^{3/2}} \right] \quad (32)$$

Using this  $f(r)$  along with the chosen pulse profile (5), we solve for the geodesics. Our numerical solutions for the geodesics are presented below in Figure (5). Throughout our analysis, we have considered  $M = 1$ .

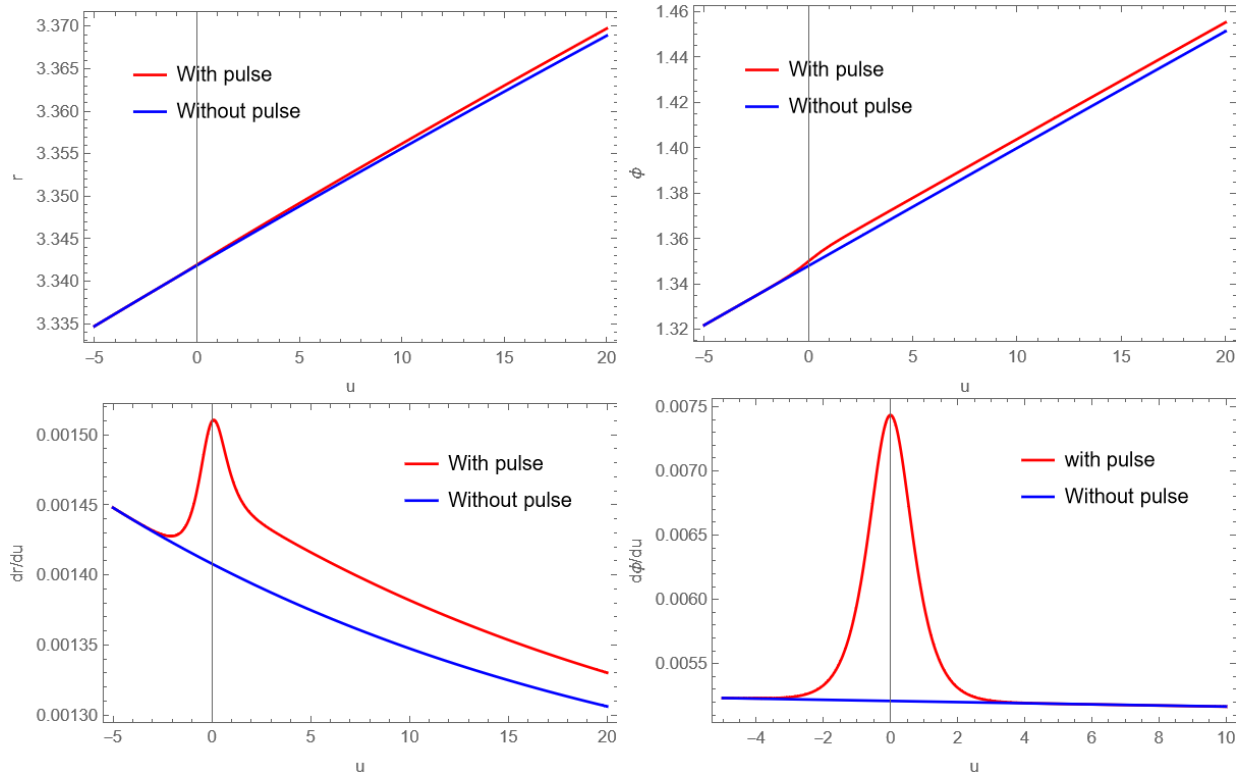


Figure 5: **Top panel:**  $r(u)$  and  $\phi(u)$  both in the presence and absence of the pulse for Bardeen Profile. **Bottom panel:** Variation of  $dr/du$  and  $d\phi/du$  with  $u$  in the presence of pulse and without pulse for Bardeen Profile. The parameters are:  $L_c = 0.1$ ,  $g = 0.1$  and  $A = 1$ .

Let us first state the initial conditions used while solving for the geodesics.

- Two geodesics are initialized at  $u = -100$ , corresponding to  $u \rightarrow -\infty$ . The initial radial coordinates are  $r[-100] = 3$  and  $r[-100] = 3.1$ .

- The initial condition for  $\phi$ ,  $dr/du$  are same as of the flat background case— i.e  $\phi[-100] = \pi/4$ ,  $p[-100] = 0.01$  for both the geodesics. The initial condition for  $q(u)$  can be fixed in the same way as done for the flat background case, thereby ensuring the timelike condition is satisfied.

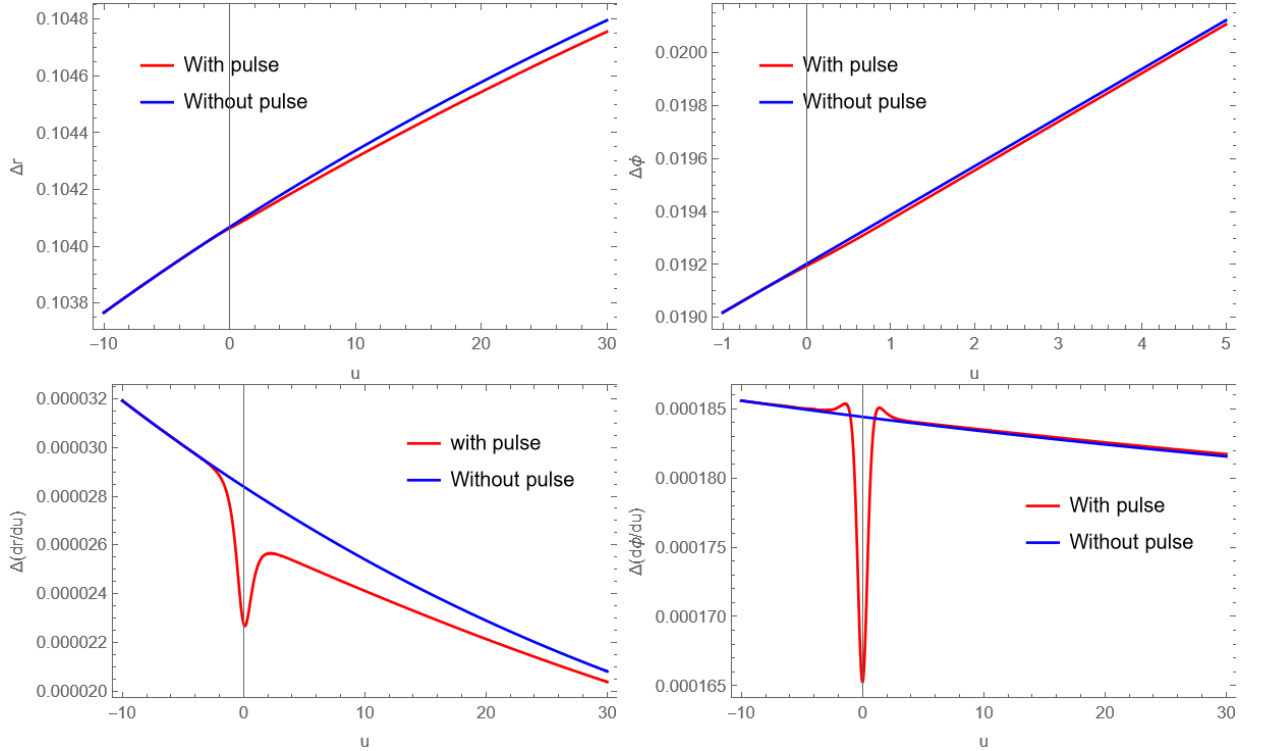


Figure 6: **Top panel:** Variation of  $\Delta r$  and  $\Delta\phi$  with  $u$  in the presence of pulse and without pulse for Bardeen profile **Bottom panel:** Variation of  $\Delta dr/du$  and  $\Delta d\phi/du$  with  $u$  in the presence of pulse and without pulse for Bardeen profile. The parameters are:  $L_c = 0.1$ ,  $g = 0.1$  and  $A = 1$ .

We now examine the evolution of the separation between two geodesics in Fig. (6) in the Bardeen spacetime. In this figure, the evolution of the separation between two nearby timelike geodesics (both  $r$  and  $\phi$  components) is plotted as a function of the  $u$  coordinate, both with and without the presence of a pulse. A clear distinction between the two scenarios, with and without the pulse, emerges at large  $u$ . This plot indicates the displacement memory in the Bardeen spacetime with a fixed  $g$  and  $L_c$ . The evolution of the tangent of the  $r$  and  $\phi$  coordinates (i.e.,  $dr/du$  and  $d\phi/du$ ) differs between the cases with and without the wave pulse. However, the magnitude of these differences are smaller than the displacement memory discussed above.

We considered  $M = 1$  and chose a wave pulse amplitude  $A = 1$ , along with  $g = 0.1$ , for Fig. (5) and Fig. (6). We have taken the initial value of  $dr/du$  as 0.01. In general, one can choose a higher initial value of  $dr/du$  and a higher  $A$ , which would also produce a noticeable displacement memory effect. To ensure that the effect of the wave pulse can be treated as a small perturbation, the amplitude  $A$  has been deliberately chosen to be small. The solution described in Eq. (32) depends on two key parameters:  $L_c$  and the regular parameter  $g$ . Changing  $g$  alters the spacetime geometry, influencing the radius of the event horizon. There exists a critical value of  $g/M$  (which we can find by setting  $g_{tt} = 0$ ) beyond which the event horizon disappears, resulting in a naked singularity. If we make the discriminant of the  $g_{tt} = 0$  to be real, we get that for  $g^2/M^2 \leq 48/81$  we will have horizons. For  $g^2/M^2 > 48/81$ , the spacetime doesn't have any event horizon, which we discarded in this discussion. Hence, we have allowed the maximum value of  $g$  to be taken up to  $\sqrt{48/81}$  (considering  $M = 1$ ).

Finally, we plot the difference between the two geodesics at positive large  $u$  ( $u \rightarrow \infty$ ) and how that changes with the variation of the  $g$  and  $L_c$  to explore how the memory depends on those parameters. That has been shown in Fig. (7) and (8). A few points corresponding to the geodesic separation analysis have been listed below :

- The differences in both  $r$  and  $\phi$  components of the two geodesics at large  $u$  decrease with increasing  $g$ , for a fixed value of  $L_c$ .

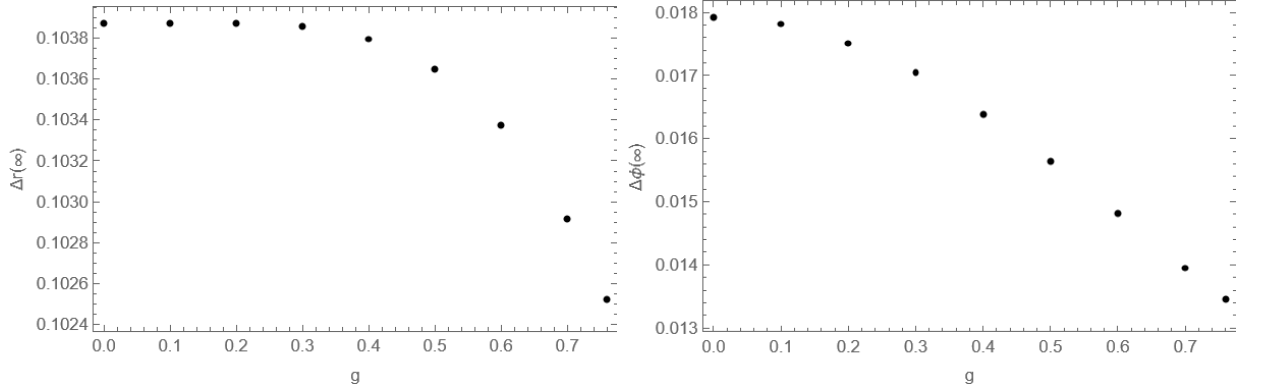


Figure. 7: Variation of  $\Delta r$  and  $\Delta\phi$  at large  $u$  with  $g$  for the Bardeen profile ( $L_c = 0.05$ ,  $A = 1$ ,  $M = 1$ ).

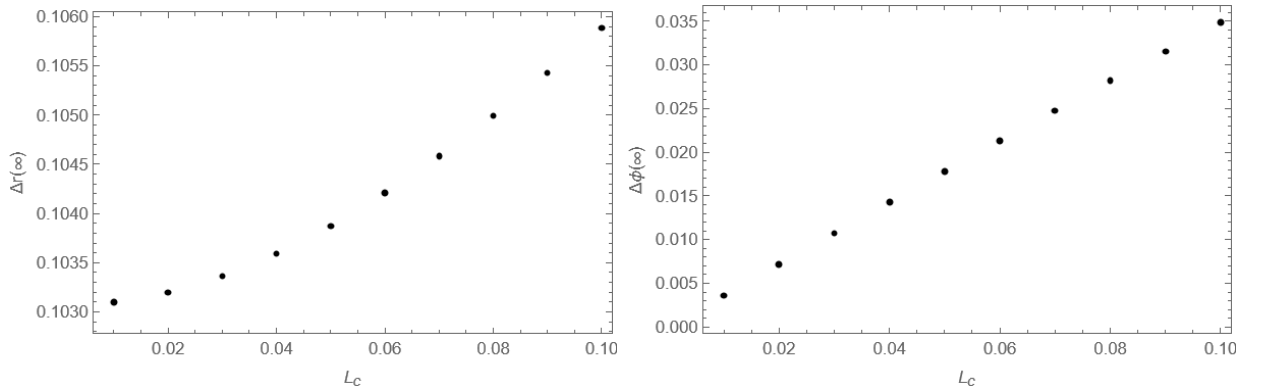


Figure. 8: Variation of  $\Delta r$  and  $\Delta\phi$  at large  $u$  with  $L_c$  for the Bardeen profile ( $g = 0.1$ ,  $A = 1$ ,  $M = 1$ ).

- In the chosen spacetime with the pulse, the conserved angular momentum ( $L_c$ ) is another parameter that is a constant motion; thus, we have studied the variation of the asymptotic  $\Delta r$  and  $\Delta\phi$  to check how the asymptotic differences depend on the values of  $L_c$  in the figure (8), and it turned out that as  $L_c$  is increased, the separation increases. This same trend for both  $L_c$  and  $g$  has been seen for other values [0.1 – 10] of the pulse amplitudes as well.
- We adopt the generalized Neves–Saa mass profile from Eq. (3), which, in the limit  $g = 0$ , reduces to the standard Schwarzschild geometry. From Fig. (7), we can note that the difference between the two geodesics is most prominent for the Schwarzschild geometry ( $g = 0$ ) for a constant  $L_c$ .

Having solved the geodesics, we now plot their trajectories. Figure (9) illustrates the trajectories under consideration.

- The left panel of Fig. (9) shows the trajectory of a particle in the  $x$ – $y$  plane in Bardeen spacetime for a fixed  $g$  and  $L_c$  value. The black curves represent the horizon, and the initial conditions are chosen such that the trajectories remain outside it, as illustrated in the figure. Each trajectory is plotted from an initial  $u = -100$  (green dot) to a final  $u = 5000$  (red dot).
- From Fig. (9), it is evident that higher values of the conserved angular momentum  $L_c$  result in trajectories that spiral outward more prominently. This behavior is consistent with Eq. (23), where an increase in  $L_c$  leads to a larger  $\dot{\phi}$ , producing faster outward spiraling, while a smaller  $L_c$  yields slower spirals closer to the central mass. Furthermore, for a fixed  $L_c$ , increasing the regular parameter widens the spiral.
- Since the spacetime contains a time-dependent pulse, it does not have a timelike Killing vector. As a result, energy is not conserved along the geodesics, and the orbits are therefore not closed.
- Our primary aim is to study the difference between trajectories as  $u \rightarrow \infty$ , which was taken to be  $u = 100$  in the previous geodesic separation analysis. At  $u = 5000$ , the  $\text{sech}^2$  function attains very small values, potentially introducing numerical errors. Therefore, we focus on the portion of the trajectory from  $u = -100$  to  $u = 100$  to analyze the memory effect in the Fig. (10).

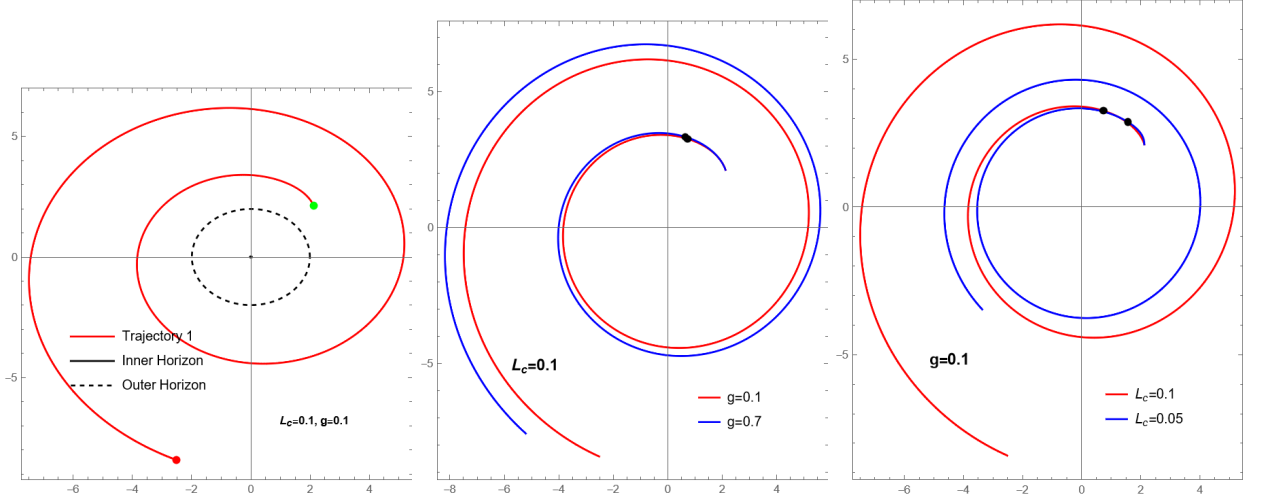


Figure 9: Trajectories in the Bardeen spacetime for different  $L_c$  and  $g$  with  $u \in [-100, 5000]$  and pulse amplitude  $A = 1$ . **Left Panel:** Trajectory of a particle in the Bardeen spacetime. The black dotted curve denotes the outer horizon. Green and red dots are the endpoints corresponding to  $u=-100$  and  $u=5000$ , respectively. **Middle Panel:** Trajectories for different  $g$  values for a fixed  $L_c$ . The black dots represent  $u = 0$  for both the trajectories. **Right panel:** Trajectories for different values of  $L_c$  at fixed  $g$ . The black dots mark  $u = 0$ .

Following the flat metric analysis, we examine the trajectories in the presence of the pulse. For  $g = 0$ , the spacetime reduces to Schwarzschild geometry. Hence, we will compare the differences in trajectories both in Schwarzschild and Bardeen spacetimes. In the Fig. (10), we have shown the two trajectories for both the Bardeen and the Schwarzschild geometry in the presence of the pulse. From the figure, it is evident that the difference between the trajectories at  $u \rightarrow \infty$  is larger than at  $u \rightarrow -\infty$ . The  $u < 0$  phase is shown in red and the  $u > 0$  phase in blue, with the trajectory starting at  $u = -100$  (red dot) and ending at  $u = +100$  (blue dot). The pulse becomes significant near  $u = 0$  (black dot). This figure also demonstrates that the separation between trajectories is larger in the Schwarzschild geometry compared to the Bardeen geometry.

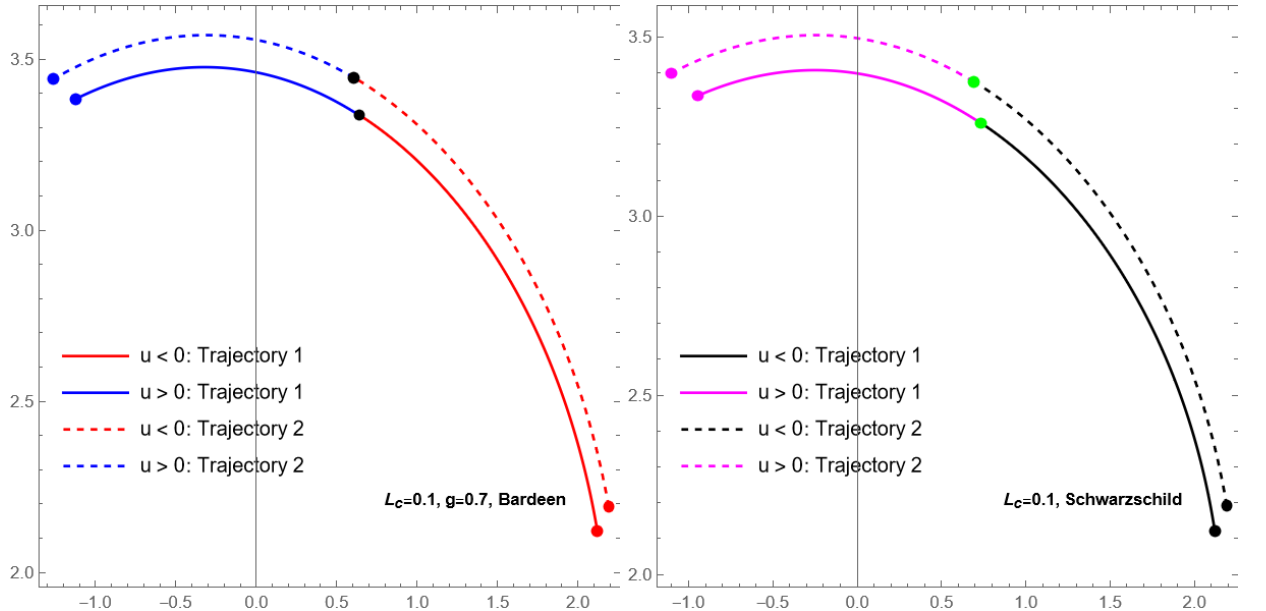


Figure 10: **Left Panel** Two trajectories (obtained from the geodesic equations using the initial conditions discussed earlier) for the Bardeen case ( $g = 0.7$ ) in the presence of the pulse. **Right Panel:** Two trajectories for the Schwarzschild case ( $g = 0$ ) in the presence of the pulse. For both cases,  $L_c = 0.1$ .

To further illustrate the above, we show the differences in the evolution of  $\Delta r$  and  $\Delta\phi$  for the Schwarzschild geometry in both the presence and absence of the pulse in the upper panel of the figure (11). The lower panel of the same figure shows that  $\Delta r$  and  $\Delta\phi$  attain larger magnitudes for the Schwarzschild geometry ( $g = 0$ ) in the presence of the pulse compared to the Bardeen geometry ( $g = 0.7$ ), for a fixed  $L_c$ . This behavior is consistent with our earlier conclusion that, for  $g = 0$ , both  $\Delta r$  and  $\Delta\phi$  are larger compared to other  $g$  values at  $u \rightarrow \infty$ . The trajectory differences at large positive  $u$  show a distinguishable measure between regular and singular black hole spacetimes. This demonstrates that the displacement memory effect might be used as an independent observational probe of black hole geometry.

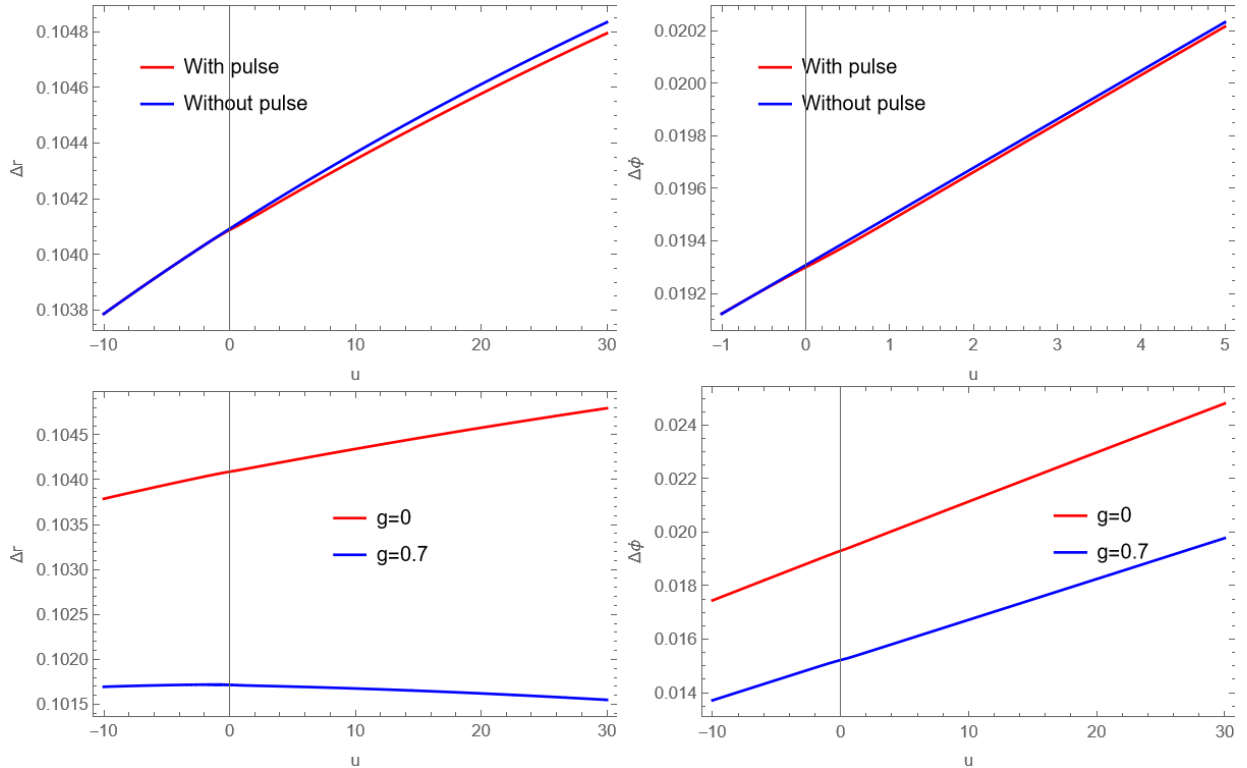


Figure. 11: **Top Panel:** Variation of  $\Delta r$  and  $\Delta\phi$  with  $u$  in the presence of pulse and without pulse for the Schwarzschild case. The parameters are  $L_c = 0.1$  and  $A = 1$ . ( $g = 0$ ). **Bottom Panel:** Evolution of  $\Delta r$  and  $\Delta\phi$  for the Schwarzschild geometry and the Bardeen geometry for a fixed  $L_c = 0.1$ , and  $A = 1$ .

### C. Analysis for the Hayward spacetime

We now move on to the Hayward regular black hole, which, like the Bardeen spacetime, reduces to Schwarzschild geometry for  $g = 0$ , and is flat for  $M = 0$ . The function  $f(r)$  for the Hayward spacetime is [80]

$$f(r) = 1 - \frac{2}{r} \left[ \frac{M}{\left(1 + \left(\frac{g}{r}\right)^3\right)} \right]. \quad (33)$$

As before, we solve Eqs. (27)–(30) using (33), with and without the pulse. The resulting geodesics as functions of  $u$  are obtained numerically and shown below in Fig. (12).

To study displacement memory in the Hayward spacetime with a pulse, we solve the geodesic equations for two different timelike geodesics and use Eq. (31) to capture their evolution as functions of  $u$ . The initial conditions, implemented at  $u = -100$ , are the same as in the Bardeen case. Figure (13) shows the radial ( $\Delta r$ ) and angular ( $\Delta\phi$ ) separations of two geodesics, with and without the pulse, as functions of  $u$ . The Hayward profile exhibits qualitative features similar to the Bardeen case. However, the memory contribution from the wave pulse is more in magnitude in

$\Delta r$  and  $\Delta\phi$ , a feature we discuss more later on. The critical value of  $g^2/M^2$  remains 48/81 for both types of spacetimes, Bardeen and Hayward.

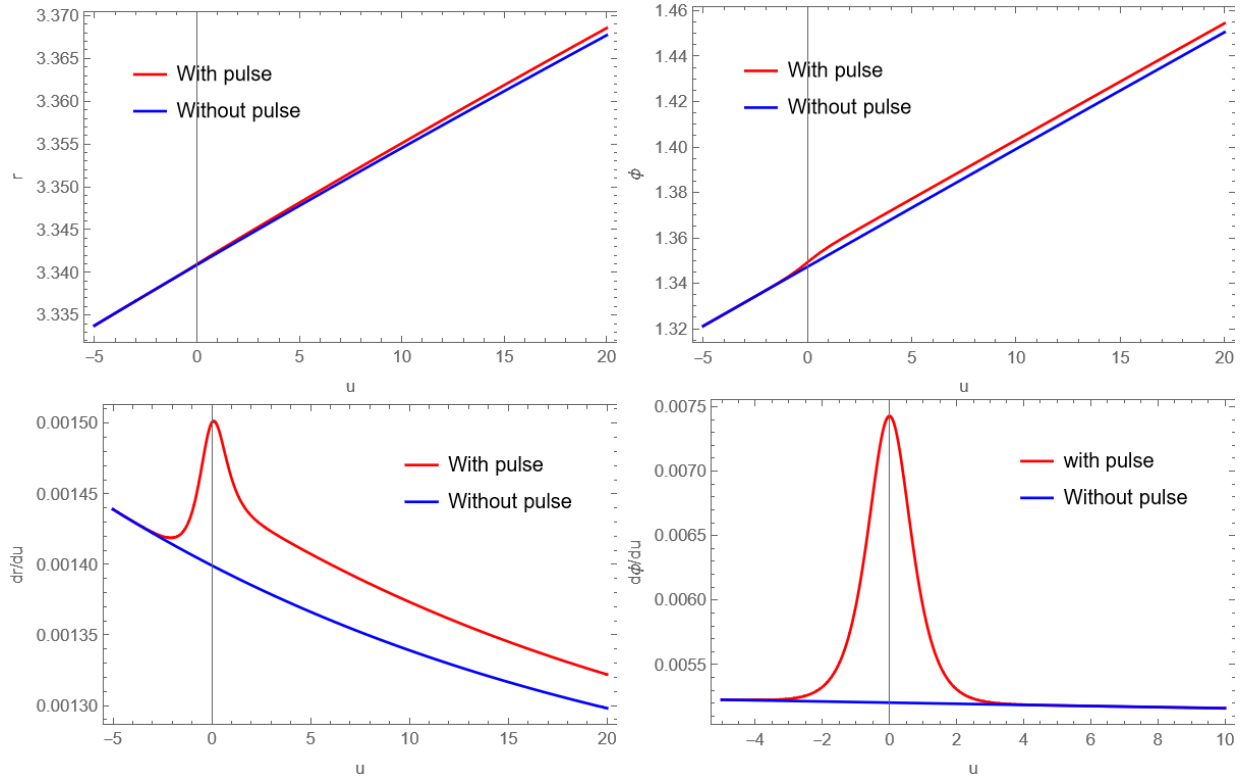


Figure 12: **Top panel:**  $r$  and  $\phi$  as functions of  $u$  in the presence and without pulse, for the Hayward Profile **Bottom panel:** Variation of  $dr/du$  and  $d\phi/du$  with  $u$  for the Hayward profile, with and without the pulse. The parameters are:  $L_c = 0.1$ ,  $g = 0.1$  and  $A = 1$ .

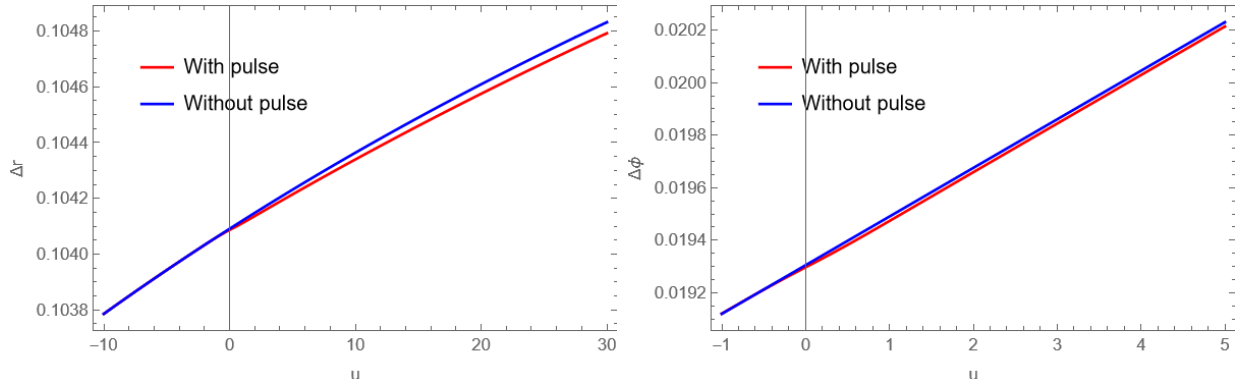


Figure 13: **Left panel:** Variation of  $\Delta r$  and  $\Delta\phi$  with  $u$  in the presence of pulse and without pulse for the Hayward profile. The parameters are:  $L_c = 0.1$ ,  $g = 0.1$ , and  $A = 1$

Analogous to the Bardeen case, we now examine the trajectories in the Hayward spacetime. The left panel of Fig. (14) shows the trajectory of the particle with the horizon of the spacetime. The trajectories remain outside the horizon and do not form closed orbits. Their dependence on  $g$  and  $L_c$  follows the same trend as in the Bardeen case. The right panel shows two trajectories in the presence of the pulse; their difference is small at  $u = -100$  but increases at  $u = 100$  due to the pulse acting near  $u = 0$  (black dot), illustrating the memory effect. The pulse acts significantly only near  $u = 0$ , while its influence is negligible in other regions.

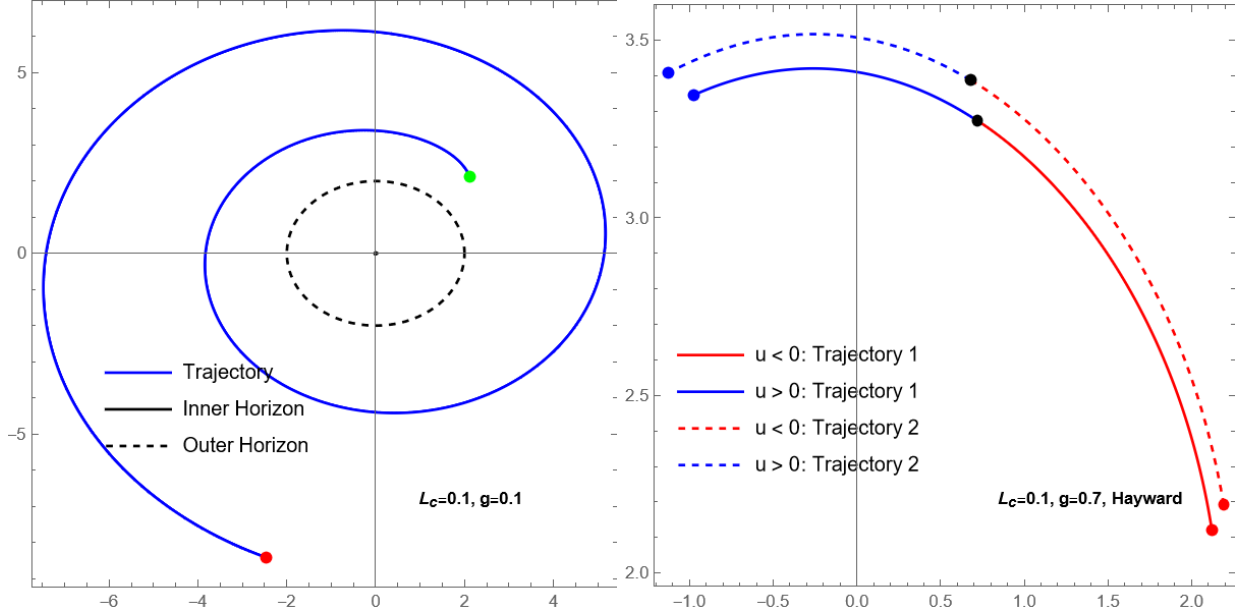


Figure. 14: **Left Panel:** Trajectory in Hayward spacetime in the presence of the pulse. The green and red dots denote  $u = -100$  and  $u = 5000$ , respectively, while the black dotted curve indicates the outer horizon. **Right panel:** Trajectories in the presence of the pulse, for  $u < 0$  (red) and  $u > 0$  (blue). The red and blue dots correspond to  $u = -100$  and  $u = 100$ , respectively, and the black dot marks  $u = 0$ , where the pulse is strongest.

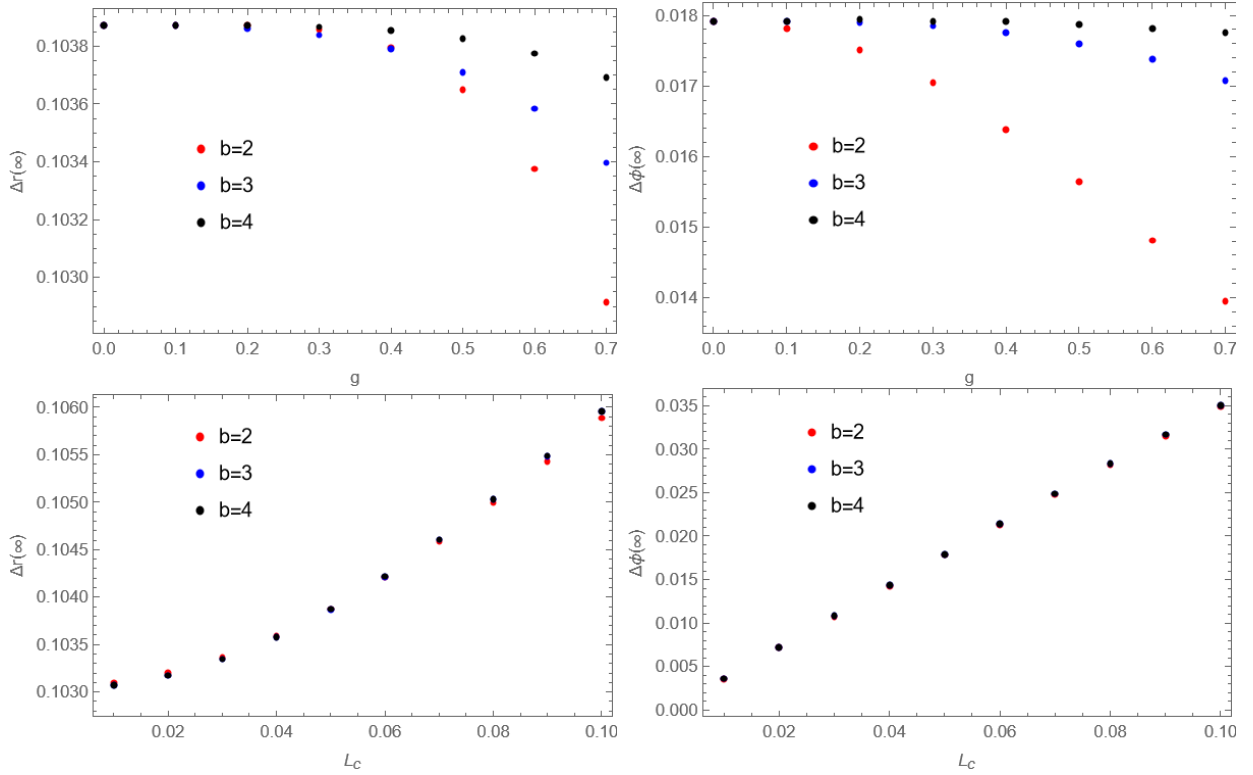


Figure. 15: **Top Panel:** Variation of the  $\Delta r$  and  $\Delta\phi$  calculated at large  $u$  with  $g$  for different values of  $b$ . The chosen parameters are:  $L_c = 0.05$  and  $A = 1$  **Bottom Panel:** Variation of the  $\Delta r$  and  $\Delta\phi$  calculated at large  $u$  with  $L_c$  for different values of  $b$ . The chosen parameters are:  $g = 0.1$  and  $A = 1$

Both the Bardeen ( $b = 2$ ) and Hayward ( $b = 3$ ) profiles follow from the general mass profile proposed by Neves and

Saa, given in Eq. (3). Setting  $g = 0$  in Eq. (3) reduces all these geometries to the Schwarzschild spacetime. As a consistency check, we compute the coordinate differences at large  $u$  ( $u = 100$ ) for the Hayward case with  $g = 0$ . We then compare these results with the corresponding Schwarzschild values. The match between them confirms the validity of our numerical analysis for the memory effect analysis. Next, we examine the dependence of the displacement memory on the parameter  $b$  of (3) in the figure (15). Our inferences from the figure (15) are mentioned below.

- At large  $u$ , the differences between geodesics vary with  $g$  and  $L_c$  in the same qualitative way. This behavior is the same for all spacetime families derived from the Neves–Saa profile.
- The analysis of the figure (15) indicates a clear trend: as the parameter  $b$  decreases, the difference between geodesics ( $r$  and  $\phi$  components) at large  $u$  decreases. Hence, the memory effect is expected to be more prominent for the Hayward spacetime compared to the Bardeen spacetime for the same set of parameters. For higher values of  $g$ , this difference is much more prominent. The difference is less at low  $g$ , whereas at higher  $g$  it is visually distinctive from the plot.
- For  $g = 0$ ,  $\Delta r(\infty)$  coincides exactly for different geometries (different  $b$  values). This is expected, since for  $g = 0$  the family of regular black hole spacetimes described by Eq. (3) reduces to the Schwarzschild geometry.
- The change in geodesic separation with respect to the regularization parameter  $g$  is more pronounced for the Bardeen profile than for other regular black holes in this family.
- Thus, for probing regular black holes with GW memory, the effect is expected to be prominent at larger  $b$  and  $L_c$  and smaller  $g$ .

#### D. Analysis for a different class of regular black holes

We now choose a different metric function  $f(r)$  [71],

$$f(r) = 1 - \frac{b_0^2 r^2}{(r^2 + g^2)^2} \quad (34)$$

Where  $b_0$  is a constant and  $g$  is the regular parameter.

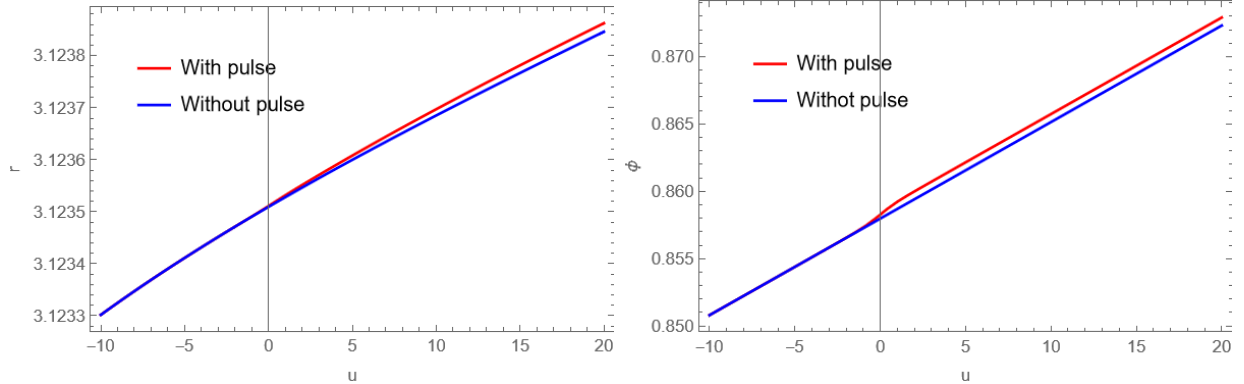


Figure 16:  $r$  and  $\phi$  components as functions of  $u$  in the presence and absence of the pulse for profile (34). The parameters are:  $L_c = 0.01$ ,  $g = 0.1$ ,  $b_0 = 1$  and  $A = 1$ .

In this  $f(r)$  too, the parameter  $g$  influences the behavior of the spacetime geometry. However, the difference to note is that this metric does not fall within the same class as the regular black hole spacetimes developed by Bardeen, Hayward, or Simpson–Visser. Such classic regular black hole solutions typically reduce to the well-known Schwarzschild geometry in the absence of the regularizing parameter—i.e., when  $g^2 = 0$ . In contrast, the  $f(r)$  above shows a different limiting behavior. When  $g^2 = 0$ , instead of recovering the singular Schwarzschild solution, the spacetime reduces to a singular and deformed version of the Reissner–Nordstrom (RN) geometry [71]. It can be shown that for  $g^2/b_0^2 > 0.25$ , there are no horizons in the geometry. Since we are not interested in geometries with no horizon, we have constrained the values of  $g$  to  $g = 0.50$ . We also choose  $b_0 = 1$ . First, we solve the coupled equations of motion using (27)–(30), using the  $f(r)$  from Eq. (34) and  $H(u)$  given in Eq. (5). Our numerical solutions are presented in the figure (16)

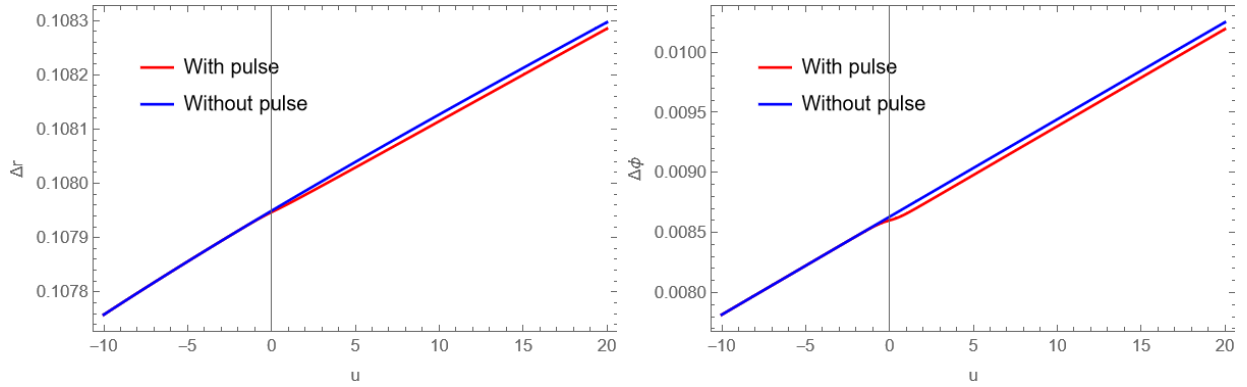


Figure. 17: **left panel:** Variation of  $\Delta r$  with  $u$  in the presence of pulse and without pulse **right panel:** Variation of  $\Delta \phi$  with  $u$  in the presence of pulse and without pulse. The chosen parameters are:  $L_c = 0.01$ ,  $g = 0.1$ , and  $A = 1$ .

For the analysis of the displacement memory effect, the same methodology as described in Section 3 is employed. Figure (17) illustrates the separation between two neighboring geodesics as a function of  $u$ , comparing cases both with and without the presence of a wave pulse. Here too, the displacement memory effect is prominent. In contrast to the profiles discussed earlier, the geodesic separation in the  $\phi$  component is notably more prominent (in magnitude) when the GW pulse is present. Examining the magnitudes of the geodesic separation, it is evident that the memory effect is larger for this profile compared to that in the previously discussed class of solutions. This might suggest that the curvature properties of this geometry tend to enhance the permanent displacement induced by the GW pulse, resulting in an increased displacement memory. To further illustrate the above feature, we explore how  $\Delta r$  and  $\Delta \phi$  at large  $u$  change with the regularization parameter  $g$  and  $L_c$  in the figure (18).

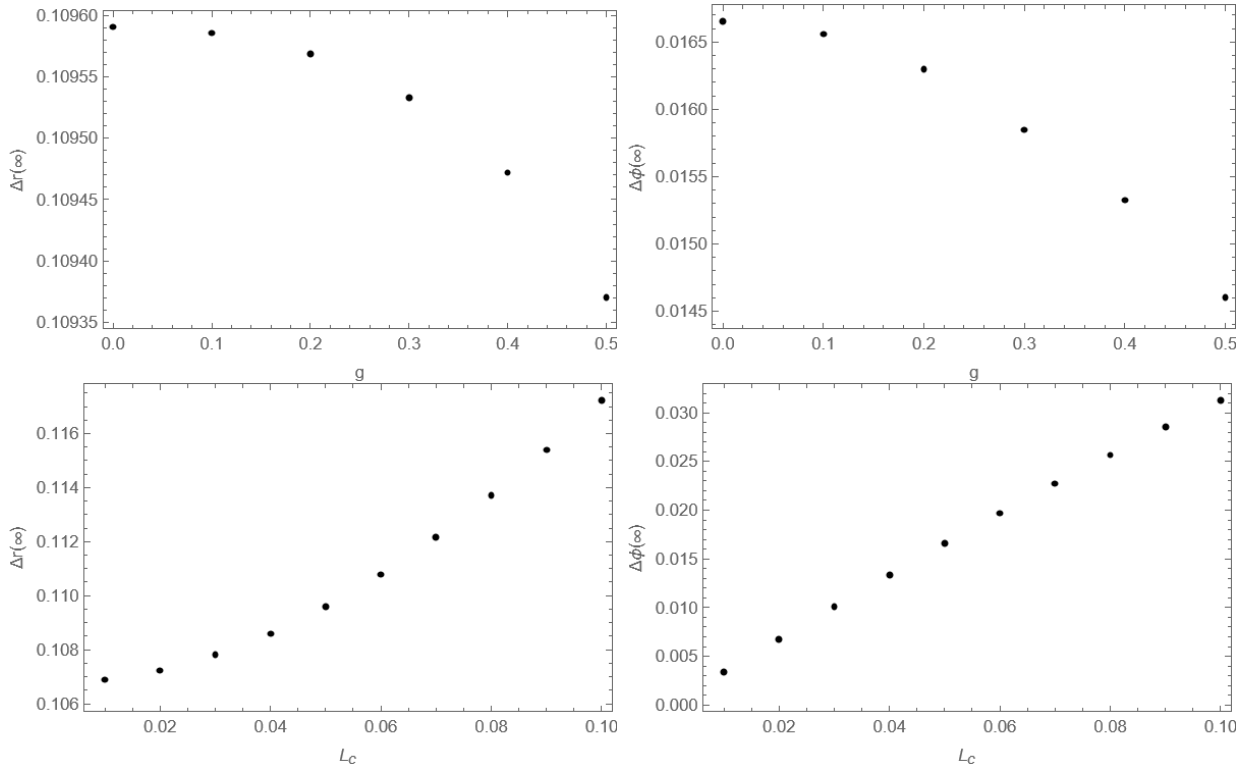


Figure. 18: **Top Panel :** Variation of  $\Delta r$  and  $\Delta \phi$  at large  $u$  with the regular parameter ( $g$ ) for the profile (34). The chosen parameters are:  $L_c = 0.05$ ,  $b_0 = 1$ , and  $A = 1$ . **Bottom Panel :** Variation of  $\Delta r$  and  $\Delta \phi$  at large  $u$  with  $L_c$ . The chosen parameters are:  $g = 0.1$ ,  $b_0 = 1$ , and  $A = 1$ .

A few points corresponding to the geodesic separation analysis for this profile are listed below:

- The differences between two geodesics in  $r$  and  $\phi$  at large  $u$  decrease with increasing  $g$ , whereas they increase

with larger values of  $L_c$ . The same trend has been observed for other regular black hole profiles as well, which we discussed earlier. Similar behaviour is noted for both  $L_c$  and  $g$  for other values (0.1 – 10) of the pulse amplitude.

- From the figure (18) it is evident that the asymptotic values of the corresponding memories are most prominent for the  $g = 0$ . We note that for  $L_c = 0.05$  and pulse amplitude  $A = 1$ , the magnitudes of the separation at large  $u$  are:

$$\Delta r(\infty) = 0.1096$$

$$\Delta\phi(\infty) = 0.0167$$

This is different from the results for Schwarzschild geometry. It is expected because the geometry does not reduce to Schwarzschild for  $g = 0$ . For the Neves–Saa cases, the magnitudes of the separation (for  $g = 0$ ) of the corresponding components at large  $u$  are

$$\Delta r(\infty) = 0.1039$$

$$\Delta\phi(\infty) = 0.0179.$$

- Thus, the memory effect carries distinct signatures in different regular black hole models, thereby providing a way to distinguish between them.

## V. GEODESIC DEVIATION AND DISPLACEMENT MEMORY

Recall the pulsed metric (in the coordinate basis) given as (4),

$$ds^2 = -f(r)du^2 - 2dudr + (r^2 + rH(u))d\theta^2 + (r^2 - rH(u))\sin^2\theta d\phi^2 \quad (35)$$

To carry out a deviation analysis, we write the deviation equation in a chosen tetrad basis as follows. The tetrad is given as:

$$e^0 = \sqrt{f(r)}du + \frac{dr}{\sqrt{f(r)}} \quad e^1 = \frac{dr}{\sqrt{f(r)}} \quad e^2 = \sqrt{r^2 + rH(u)}d\theta \quad e^3 = \sqrt{r^2 - rH(u)}\sin\theta d\phi, \quad (36)$$

and the coordinate basis is given as,

$$e^{0'} = du \quad e^{1'} = dr \quad e^{2'} = d\theta \quad e^{3'} = d\phi \quad (37)$$

Furthermore, we restrict our attention to geodesics lying in the equatorial plane, i.e.,  $\theta = \pi/2$ . The deviation vector components are computed with respect to the numerically obtained geodesics, as discussed in the earlier sections of this article. The explicit expressions for the non-vanishing components of the Riemann tensor are provided in Appendix A. For the geodesic deviation equations, the indices 0, 1, 2, 3 correspond to the coordinates in tetrad basis, which we adopt for our analysis.

In the previous section, we derived and solved the geodesic equations in the  $u$  coordinate. Following the same approach, we now express the geodesic deviation equations in terms of  $u$ , making use of (24) and (26). All relevant Riemann tensor components must be evaluated along the numerically obtained geodesics. Accordingly, we rewrite the deviation equations in the  $u$  coordinate and solve them numerically for different parameter choices corresponding to the different geometries. The deviation equation reduces to the following set of equations,

$$\frac{d^2\eta^0}{du^2} + \frac{d\eta^0}{du} \left( \frac{f'(r)}{2} + \frac{f(r) + 2p(u)}{1 + \frac{L_c^2}{r^2 - rH}} \frac{H - 2r}{2} \frac{L_c^2}{(r^2 - rH)^2} \right) = -R_{003}^0 \eta^0 q(u)^2 - R_{013}^0 \eta^1 q(u)^2 + R_{003}^0 \eta^3 q(u) + R_{013}^0 \eta^3 p(u)q(u) \quad (38)$$

$$\begin{aligned} \frac{d^2\eta^1}{du^2} + \frac{d\eta^1}{du} \left( \frac{f'(r)}{2} + \frac{f(r) + 2p(u)}{1 + \frac{L_c^2}{r^2 - rH}} \frac{H - 2r}{2} \frac{L_c^2}{(r^2 - rH)^2} \right) = & -R_{001}^1 \eta^0 p(u) - R_{303}^1 \eta^0 q(u)^2 \\ & - R_{010}^1 \eta^1 - R_{313}^1 \eta^1 q(u)^2 - R_{330}^1 \eta^3 q(u) - R_{331}^1 \eta^3 p(u)q(u) \end{aligned} \quad (39)$$

$$\frac{d^2\eta^2}{du^2} + \frac{d\eta^2}{du} \left( \frac{f'(r)}{2} + \frac{f(r) + 2p(u)}{1 + \frac{L_c^2}{r^2 - rH}} \frac{H - 2r}{2} \frac{L_c^2}{(r^2 - rH)^2} \right) = -R_{020}^2\eta^2 - R_{021}^2\eta^2p(u) - R_{120}^2\eta^2p(u) - R_{121}^2\eta^2p(u)^2 - R_{323}^2\eta^2q(u)^2 \quad (40)$$

$$\frac{d^2\eta^3}{du^2} + \frac{d\eta^3}{du} \left( \frac{f'(r)}{2} + \frac{f(r) + 2p(u)}{1 + \frac{L_c^2}{r^2 - rH}} \frac{H - 2r}{2} \frac{L_c^2}{(r^2 - rH)^2} \right) = -R_{003}^3\eta^0q(u) - R_{103}^3\eta^0p(u)q(u) - R_{013}^3\eta^1q(u) - R_{113}^3\eta^1p(u)q(u) - R_{030}^3\eta^3 - R_{031}^3\eta^3p(u) - R_{130}^3\eta^3p(u) - R_{131}^3\eta^3p(u)^2. \quad (41)$$

Here,  $p(u) = \frac{dr}{du}$  and  $q(u) = \frac{d\phi}{du}$ . The functions  $r(u)$ ,  $\phi(u)$ ,  $p(u)$ , and  $q(u)$  have already been obtained in the geodesic analysis for different geometries. We now use those numerical solutions to integrate Eqs.(38)–(41), using appropriate initial conditions and parameter choices for different geometries. The solutions obtained in the tetrad basis are then transformed back into the coordinate basis in order to facilitate a direct qualitative comparison with the earlier geodesic analysis, which was performed in the coordinate basis. The numerical results for the  $r$  and  $\phi$  components of the deviation vector are presented in the following sections, where we emphasize the comparative features of the deviation behavior across different spacetime geometries.

### A. Flat Metric

We solve Eqs. (38)–(41) for the flat metric, where  $f(r) = 1$ . The geodesics for this case have already been computed numerically in the earlier section. We now use those solutions to first write down and then numerically integrate the deviation equation. The initial conditions are listed in Table I. These conditions are chosen to enable a qualitative comparison between the  $r$  and  $\phi$  components of the geodesic separation and the geodesic deviation vector.

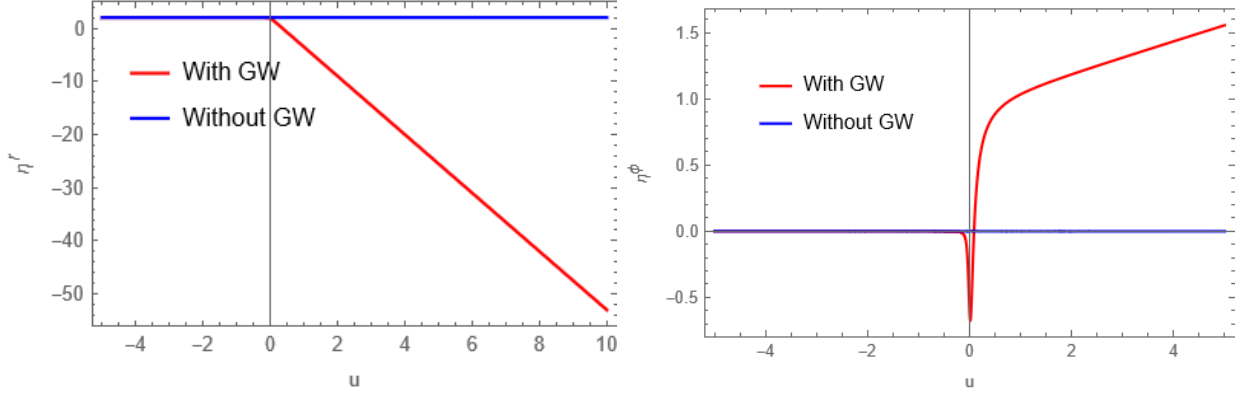


Figure 19:  $r$  and  $\phi$  components of the deviation vector in the flat metric, both in the presence and in the absence of the pulse. The parameters are:  $L_c = 0.005$ ,  $A = 3$ .

Quantity	Value at $u = -100$
$\eta^u, \eta^\theta, \eta^\phi$	0
$\frac{d\eta^u}{du}, \frac{d\eta^r}{du}, \frac{d\eta^\theta}{du}, \frac{d\eta^\phi}{du}$	0
$\eta^r$	2

Table. I: Initial conditions for solving the deviation equations in the flat metric.

Figure (19) shows the numerical results for the  $r$  and  $\phi$  components of the deviation vector as functions of  $u$ . The qualitative behaviour of the  $r$ -component is consistent with that obtained from the geodesic separation analysis, whereas the  $\phi$ -component exhibits distinct features in the transient region. Here, we observe that the corresponding components of the deviation vector begin to evolve differently in the two scenarios—with and without the GW pulse—from  $u = 0$ ,

the region where the effect of the pulse is introduced. At large values of  $u$ , the deviation vector exhibits a lasting difference between the two cases, which corresponds to the displacement memory effect.

### B. Bardeen Profile

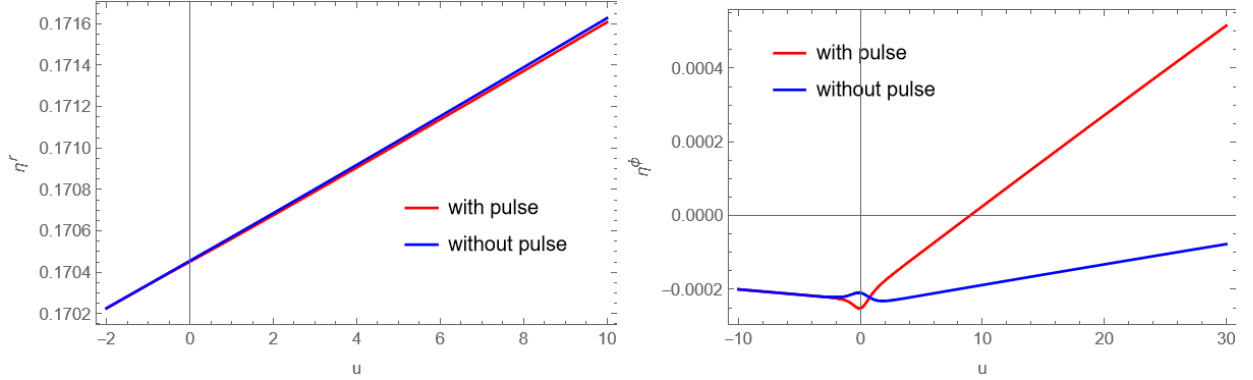


Figure. 20:  $r$  and  $\phi$  component of the deviation vector in case of Bardeen metric, both in the presence and in the absence of the pulse. The parameters are:  $g = 0.1$ ,  $L_c = 0.1$ ,  $A = 1$ ,  $m = 1$

For the Bardeen profile,  $f(r)$  is given by (32). We plot the  $r$  and  $\phi$  components of the deviation vectors in the figure (20). The initial conditions are the same as in the flat metric case (Table I), except for  $\eta^r[-100] = 0.1$ . Here, also, the  $r$ -component shows qualitative similarity with the separation vector  $\Delta r$ , while the  $\phi$ -component exhibits a different behaviour, Fig. (6).

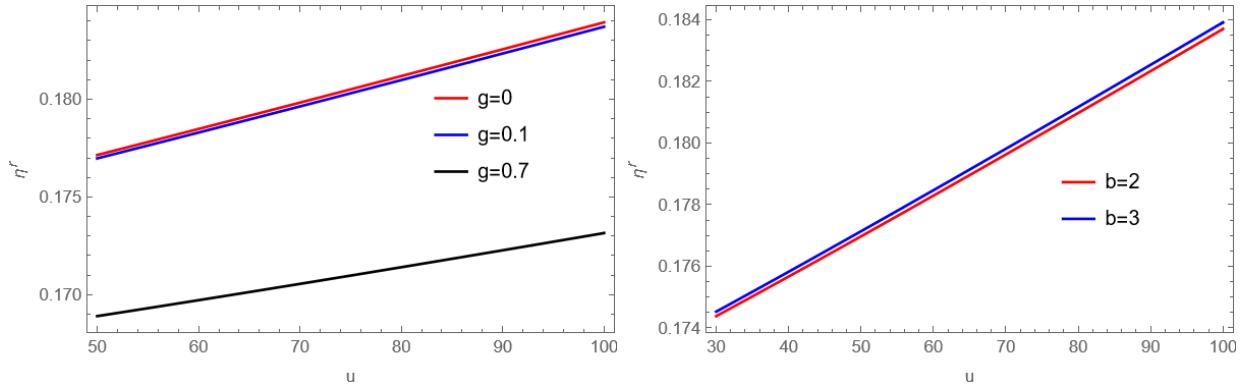


Figure. 21: **Left panel:**  $r$  component of deviation vector for different values of  $g$  with  $L_c = 0.1$  and  $A = 1$ . **Right panel**  $r$  component of deviation vector for different values of  $b$  with  $L_c = 0.1$ ,  $g = 0.1$ , and  $A = 1$ .

In Fig. (21), we show the  $r$ -component of the deviation vector for different values of  $g$  and  $b$ . In the geodesic separation analysis, we found that  $\Delta r$  at large  $u$  for the Schwarzschild case ( $g = 0$ ), is larger compared to that for the regular black hole cases. The left panel of Fig. (21) confirms this behaviour, showing that the  $r$ -component of the deviation vector is indeed larger in magnitude for  $g = 0$  than for nonzero  $g$ . Furthermore, the memory effect is smaller for nonzero lower values of  $g$ . The dependence on  $b$  is also shown in the right panel, where larger values of  $b$  correspond to larger values of  $\eta^r$ . Overall, the dependence of the memory on these parameters confirms that the deviation analysis and the geodesic analysis are qualitatively consistent, as they are expected to be. We note that while the radial ( $r$ ) component of the separation and the deviation vector exhibit nearly identical qualitative behavior, the  $\phi$  component displays a transient that differs between the two approaches. This discrepancy may be understood as follows. The geodesic separation method involves two geodesics that are not necessarily infinitesimally close whereas the deviation–vector analysis always assumes infinitesimal deviations about a central geodesic. Thus, while both the deviation–vector and geodesic–separation methods yield the same qualitative behaviour at large  $u$ , they differ at small  $u$ , as manifest in the  $\eta^\phi$  component.

## VI. CONCLUSION

In this work, we have investigated the displacement memory effect in regular black hole spacetimes using geodesic separation and geodesic deviation. Our main findings may be summarized as follows:

### 1. Studies on the memory effect:

- The separation between two geodesics after the pulse passes differs between the cases with and without the pulse. This demonstrates that the wave pulse leaves a permanent imprint, known as displacement memory. Both geodesic separation and geodesic deviation analyses consistently show that a wave pulse induces a permanent displacement at large  $u$ .
- The qualitative behavior of the  $r$  coordinate at large  $u$  is in good agreement between the two approaches, whereas the transient behavior of the  $\phi$  component differs.

### 2. Parameter dependence:

- Displacement memory depends on the regularization parameter  $g$ , the angular momentum  $L_c$ , and the pulse profile parameter  $b$ .
- The magnitude of displacement memory decreases with increasing  $g$ , while it increases with larger  $L_c$  and  $b$ .
- The Schwarzschild limit ( $g = 0$ ) yields the largest memory, marking a clear distinction between singular and regular black hole geometries. This suggests that the memory effect can serve as a tool to distinguish regular black hole models from the singular Schwarzschild spacetime. It may also be used to differentiate between various regular black hole models.

### 3. Comparison across regular black hole geometries:

- The Bardeen, Hayward, and related Neves–Saa profiles exhibit distinct signatures which are manifest through the magnitude of displacement memory.
- A different class of regular black holes (34) shows even stronger memory effects, highlighting how curvature variations also influence permanent displacements.
- Such characteristic variations indicate that memory could be exploited to distinguish between different families of regular black holes.

From both geodesic separation and geodesic deviation analyses, we find that the memory effect depends on the regularization parameter  $g$ . Consequently, following the Bondi–Sachs analysis, the Bondi functions are expected to reflect this dependence. To observe the influence of  $g$  on the Bondi mass and parameters, the asymptotic expansion of the mass function (3) must include  $g$  in the  $1/r$  or  $1/r^2$  terms:

$$m(r) \simeq M \left[ 1 - \left( \frac{a}{b} \right) \left( \frac{g}{r} \right)^b + \frac{a/b(a/b+1)}{2} \left( \frac{g}{r} \right)^{2b} - \dots \right], \quad f(r) = 1 - \frac{2m(r)}{r}. \quad (42)$$

It follows that  $g$  affects the Bondi functions only if  $b \leq 1$ . Choosing  $a = b = 1$ , the large- $r$  metric becomes

$$ds^2 = - \left( 1 - \frac{2M}{r} + \frac{2Mg^2}{r^2} \right) du^2 - 2dudr + r^2 d\Omega^2. \quad (43)$$

Within the Bondi–Sachs framework,  $g$  explicitly enters the subleading asymptotic terms, directly linking the geodesic memory effect to asymptotic flux-balance laws at large  $u$ . We have performed a complete analysis of the  $g$ -dependence in the Bondi functions (for  $b = 1$ ), but do not report it here, as  $g$  contributes only at subleading order for  $b = 1$ . For the regular black holes considered in our work—for example, Bardeen ( $b = 2$ ) and Hayward ( $b = 3$ )—the  $g$ -dependence appears in even higher-order Bondi terms and is therefore negligible.

The present study establishes that gravitational wave memory carries distinct imprints related to the background black hole geometry and its regular or singular nature. Looking ahead, several avenues remain open:

- Extending the analysis to *nonlinear (Christodoulou) memory* and *tail effects* could provide a more complete picture of memory in regular spacetimes. A perturbative analysis could reveal higher-order effects, enhancing both theoretical insight and potential observational relevance.
- Incorporating *realistic astrophysical sources* of gravitational radiation, such as binary mergers in regular black hole backgrounds, would enhance the observational relevance of these results.

## ACKNOWLEDGEMENTS

RA thanks the Indian Institute of Technology Kharagpur, India, for supporting him through a fellowship allowing access to available computational facilities.

- 
- [1] B. P. Abbott, R. Abbott, T. D. Abbott, M. R. Abernathy, F. Acernese, K. Ackley, C. Adams, T. Adams, P. Addesso, R. X. Adhikari, et al. (LIGO Scientific Collaboration and Virgo Collaboration), *Phys. Rev. Lett.* **116**, 061102 (2016), URL <https://link.aps.org/doi/10.1103/PhysRevLett.116.061102>.
- [2] T. L. S. Collaboration, T. V. Collaboration, T. K. Collaboration, and Others, *Gw230814: investigation of a loud gravitational-wave signal observed with a single detector* (2025), 2509.07348, URL <https://arxiv.org/abs/2509.07348>.
- [3] A. Akyüz, A. Correia, J. Garofalo, K. Kacanja, L. Roy, K. Soni, H. Tan, V. J. Y. A. H. Nitz, and C. D. Capano, *Potential science with gw250114 – the loudest binary black hole merger detected to date* (2025), 2507.08789, URL <https://arxiv.org/abs/2507.08789>.
- [4] B. P. Abbott, R. Abbott, T. D. Abbott, F. Acernese, K. Ackley, C. Adams, T. Adams, P. Addesso, R. X. Adhikari, V. B. Adya, et al. (LIGO Scientific Collaboration and Virgo Collaboration), *Phys. Rev. Lett.* **119**, 161101 (2017), URL <https://link.aps.org/doi/10.1103/PhysRevLett.119.161101>.
- [5] L. Rezzolla, *Gravitational waves from perturbed black holes and relativistic stars* (2003), gr-qc/0302025, URL <https://arxiv.org/abs/gr-qc/0302025>.
- [6] S. Mastrogiovanni, D. A. Steer, and M. Barsuglia, *Phys. Rev. D* **102**, 044009 (2020), URL <https://link.aps.org/doi/10.1103/PhysRevD.102.044009>.
- [7] S. Shankaranarayanan and J. P. Johnson, *General Relativity and Gravitation* **54** (2022), ISSN 1572-9532, URL <http://dx.doi.org/10.1007/s10714-022-02927-2>.
- [8] T. Hinderer, *The Astrophysical Journal* **677**, 1216 (2008), URL <https://doi.org/10.1086/533487>.
- [9] B. Wang, Z. Zhu, A. Li, and W. Zhao, *The Astrophysical Journal Supplement Series* **250**, 6 (2020), URL <https://doi.org/10.3847/1538-4365/aba2f3>.
- [10] N. Jiang and K. Yagi, *Phys. Rev. D* **103**, 124047 (2021), URL <https://link.aps.org/doi/10.1103/PhysRevD.103.124047>.
- [11] M. Favata, *Phys. Rev. D* **80**, 024002 (2009), URL <https://link.aps.org/doi/10.1103/PhysRevD.80.024002>.
- [12] M. Favata, *Classical and Quantum Gravity* **27**, 084036 (2010), ISSN 1361-6382, URL <http://dx.doi.org/10.1088/0264-9381/27/8/084036>.
- [13] M. Favata, *Phys. Rev. D* **84**, 124013 (2011), URL <https://link.aps.org/doi/10.1103/PhysRevD.84.124013>.
- [14] L. Heisenberg, N. Yunes, and J. Zosso, *Physical Review D* **108** (2023), ISSN 2470-0029, URL <http://dx.doi.org/10.1103/PhysRevD.108.024010>.
- [15] M. Hübner, P. Lasky, and E. Thrane, *Phys. Rev. D* **104**, 023004 (2021), URL <https://link.aps.org/doi/10.1103/PhysRevD.104.023004>.
- [16] Y. B. Zel'dovich and A. G. Polnarev, *Sov. Astron.* **18**, 17 (1974).
- [17] V. B. Braginsky and L. P. Grishchuk, *Sov. Phys. JETP* **62**, 427 (1985).
- [18] D. Christodoulou, *Phys. Rev. Lett.* **67**, 1486 (1991), URL <https://link.aps.org/doi/10.1103/PhysRevLett.67.1486>.
- [19] K. S. Thorne, *Phys. Rev. D* **45**, 520 (1992), URL <https://link.aps.org/doi/10.1103/PhysRevD.45.520>.
- [20] A. G. Wiseman and C. M. Will, *Phys. Rev. D* **44**, R2945 (1991), URL <https://link.aps.org/doi/10.1103/PhysRevD.44.R2945>.
- [21] L. Bieri and D. Garfinkle, *Phys. Rev. D* **89**, 084039 (2014), URL <https://link.aps.org/doi/10.1103/PhysRevD.89.084039>.
- [22] A. Tolish, L. Bieri, D. Garfinkle, and R. M. Wald, *Phys. Rev. D* **90**, 044060 (2014), URL <https://link.aps.org/doi/10.1103/PhysRevD.90.044060>.
- [23] A. M. Grant and D. A. Nichols, *Phys. Rev. D* **107**, 064056 (2023), URL <https://link.aps.org/doi/10.1103/PhysRevD.107.064056>.
- [24] L. Bieri and A. Polnarev, *Class. Quant. Grav.* **41**, 135012 (2024), 2402.02594.
- [25] S. Bhattacharya and S. Ghosh, *Displacement memory and b-memory in generalised ellis-bronnikov wormholes* (2025), 2502.03007, URL <https://arxiv.org/abs/2502.03007>.
- [26] L. P. Grishchuk and A. G. Polnarev, *Sov. Phys. JETP* **69**, 653 (1989).
- [27] P.-M. Zhang, C. Duval, G. Gibbons, and P. Horvathy, *Journal of Cosmology and Astroparticle Physics* **2018**, 030–030 (2018), ISSN 1475-7516, URL <http://dx.doi.org/10.1088/1475-7516/2018/05/030>.
- [28] S. Pasterski, A. Strominger, and A. Zhiboedov, *JHEP* **12**, 053 (2016), 1502.06120.
- [29] D. A. Nichols, *Phys. Rev. D* **95**, 084048 (2017), 1702.03300.
- [30] L. Bieri, P. Chen, and S.-T. Yau, *Classical and Quantum Gravity* **29**, 215003 (2012), ISSN 1361-6382, URL <http://dx.doi.org/10.1088/0264-9381/29/21/215003>.
- [31] J. Winicour, *Classical and Quantum Gravity* **31**, 205003 (2014), ISSN 1361-6382, URL <http://dx.doi.org/10.1088/0264-9381/31/20/205003>.
- [32] P. Mao, *Phys. Rev. D* **104**, 084026 (2021), URL <https://link.aps.org/doi/10.1103/PhysRevD.104.084026>.
- [33] É. É. Flanagan, A. M. Grant, A. I. Harte, and D. A. Nichols, *Physical Review D* **99**, 084044 (2019).

- [34] É. É. Flanagan, A. M. Grant, A. I. Harte, and D. A. Nichols, Phys. Rev. D **101**, 104033 (2020), 1912.13449.
- [35] R. R. Caldwell, *The persistence of nonlinear gravitational wave memory* (2025), 2506.20751, URL <https://arxiv.org/abs/2506.20751>.
- [36] K. Cunningham, C. Kavanagh, A. Pound, D. Trestini, N. Warburton, and J. Neef, Classical and Quantum Gravity **42**, 199401 (2025), URL <https://doi.org/10.1088/1361-6382/ae09e8>.
- [37] P.-M. Zhang, C. Duval, G. Gibbons, and P. Horvathy, Physics Letters B **772**, 743 (2017), ISSN 0370-2693, URL <https://www.sciencedirect.com/science/article/pii/S0370269317306068>.
- [38] M. O'Loughlin and H. Demirchian, Phys. Rev. D **99**, 024031 (2019), URL <https://link.aps.org/doi/10.1103/PhysRevD.99.024031>.
- [39] I. Chakraborty and S. Kar, The European Physical Journal Plus **137** (2022), ISSN 2190-5444, URL <http://dx.doi.org/10.1140/epjp/s13360-022-02593-y>.
- [40] A. Tolish and R. Wald, Physical Review D **94** (2016).
- [41] I. Chakraborty, S. Jana, and S. Shankaranarayanan, *Prospects for cosmological constraints using gravitational wave memory* (2025), 2402.18083, URL <https://arxiv.org/abs/2402.18083>.
- [42] A. Strominger and A. Zhiboedov, JHEP **01**, 086 (2016), 1411.5745.
- [43] L. Blanchet, G. Compère, G. Faye, R. Oliveri, and A. Seraj, Journal of High Energy Physics **2023** (2023), ISSN 1029-8479, URL [http://dx.doi.org/10.1007/JHEP07\(2023\)123](http://dx.doi.org/10.1007/JHEP07(2023)123).
- [44] D. N. Solanki and S. Bhattacharjee, Eur. Phys. J. C **83**, 1167 (2023), 2308.02445.
- [45] R. K. Singh, S. Kumar, A. Chowdhuri, and A. Bhattacharyya, *Gravitational memory meets astrophysical environments: exploring a new frontier through osculations* (2025), 2509.01676, URL <https://arxiv.org/abs/2509.01676>.
- [46] Q. Alnasheet, V. Cardoso, F. Duque, and R. P. Macedo, Phys. Rev. D **112**, 044066 (2025), URL <https://link.aps.org/doi/10.1103/yyv5-3y1c>.
- [47] D. Pollney and C. Reisswig, Astrophys. J. Lett. **732**, L13 (2011), 1004.4209.
- [48] K. Mitman, J. Moxon, M. A. Scheel, S. A. Teukolsky, M. Boyle, N. Deppe, L. E. Kidder, and W. Throwe, Phys. Rev. D **102**, 104007 (2020), 2007.11562.
- [49] K. Mitman et al., Phys. Rev. D **104**, 024051 (2021), 2105.02300.
- [50] K. Mitman et al., Phys. Rev. D **106**, 084029 (2022), 2208.04356.
- [51] K. Mitman, M. Boyle, L. C. Stein, N. Deppe, L. E. Kidder, J. Moxon, H. P. Pfeiffer, M. A. Scheel, S. A. Teukolsky, W. Throwe, et al., Classical and Quantum Gravity **41**, 223001 (2024), ISSN 1361-6382, URL <http://dx.doi.org/10.1088/1361-6382/ad83c2>.
- [52] M. Favata, Journal of Physics: Conference Series **154**, 012043 (2009), URL <https://dx.doi.org/10.1088/1742-6596/154/1/012043>.
- [53] E. Grilli, A. Placidi, S. Albanesi, G. Grignani, and M. Orselli, Phys. Rev. D **111**, 044045 (2025), URL <https://link.aps.org/doi/10.1103/PhysRevD.111.044045>.
- [54] P. D. Lasky, E. Thrane, Y. Levin, J. Blackman, and Y. Chen, Phys. Rev. Lett. **117**, 061102 (2016), URL <https://link.aps.org/doi/10.1103/PhysRevLett.117.061102>.
- [55] C. Talbot, E. Thrane, P. D. Lasky, and F. Lin, Phys. Rev. D **98**, 064031 (2018), 1807.00990.
- [56] K. Islo, J. Simon, S. Burke-Spoliar, and X. Siemens (2019), 1906.11936.
- [57] M. Hübner, C. Talbot, P. D. Lasky, and E. Thrane, Phys. Rev. D **101**, 023011 (2020), URL <https://link.aps.org/doi/10.1103/PhysRevD.101.023011>.
- [58] B. Goncharov, L. Donnay, and J. Harms, Phys. Rev. Lett. **132**, 241401 (2024), 2310.10718.
- [59] H. Inchauspé, S. Gasparotto, D. Blas, L. Heisenberg, J. Zosso, and S. Tiwari, *Measuring gravitational wave memory with lisa* (2024), 2406.09228, URL <https://arxiv.org/abs/2406.09228>.
- [60] A. Elhashash and D. A. Nichols, *Waveform models for the gravitational-wave memory effect: Ii. time-domain and frequency-domain models for nonspinning binaries* (2025), 2504.18635, URL <https://arxiv.org/abs/2504.18635>.
- [61] G. Agazie, A. Anumarlapudi, A. M. Archibald, Z. Arzoumanian, J. G. Baier, P. T. Baker, B. Becsy, L. Blecha, A. Brazier, P. R. Brook, et al., *The nanograv 15-year data set: Search for gravitational wave memory* (2025), 2502.18599, URL <https://arxiv.org/abs/2502.18599>.
- [62] H. Inchauspé, S. Gasparotto, D. Blas, L. Heisenberg, J. Zosso, and S. Tiwari, Phys. Rev. D **111**, 044044 (2025), URL <https://link.aps.org/doi/10.1103/PhysRevD.111.044044>.
- [63] G. Shore, Nuclear Physics B **605**, 455–466 (2001), ISSN 0550-3213, URL [http://dx.doi.org/10.1016/S0550-3213\(01\)00137-7](http://dx.doi.org/10.1016/S0550-3213(01)00137-7).
- [64] I. Chakraborty, S. Bhattacharya, and S. Chakraborty, Phys. Rev. D **106**, 104057 (2022), URL <https://link.aps.org/doi/10.1103/PhysRevD.106.104057>.
- [65] S. Datta and S. Guha, Physica Scripta **99**, 075023 (2024), ISSN 1402-4896, URL <http://dx.doi.org/10.1088/1402-4896/ad5389>.
- [66] H. Hadi, A. Rezaei Akbarieh, and D. F. Mota, Classical and Quantum Gravity **41**, 105005 (2024), ISSN 1361-6382, URL <http://dx.doi.org/10.1088/1361-6382/ad3caf>.
- [67] A. D. Sakharov, Soviet Journal of Experimental and Theoretical Physics **22**, 241 (1966).
- [68] E. B. Gliner, Soviet Journal of Experimental and Theoretical Physics **22**, 378 (1966).
- [69] P. S. Joshi, *Spacetime Singularities* (Springer Berlin Heidelberg, 2014), p. 409–436, ISBN 9783642419928, URL [http://dx.doi.org/10.1007/978-3-642-41992-8\\_20](http://dx.doi.org/10.1007/978-3-642-41992-8_20).
- [70] M. Novello and S. Bergliaffa, Physics Reports **463**, 127–213 (2008), ISSN 0370-1573, URL <http://dx.doi.org/10.1016/j.physrep.2008.04.006>.

- [71] A. Kar and S. Kar, *Gen. Rel. Grav.* **56**, 52 (2024), 2308.12155.
- [72] H. Huang and X.-P. Rao, *Regular black holes and their singular families* (2025), 2503.13133, URL <https://arxiv.org/abs/2503.13133>.
- [73] A. Kar and S. Kar, *Eur. Phys. J. C* **85**, 773 (2025), 2504.12042.
- [74] P. Bueno, P. A. Cano, R. A. Hennigar, Ángel J. Murcia, and A. Vicente-Cano, *Regular black holes from oppenheimer-snyder collapse* (2025), 2505.09680, URL <https://arxiv.org/abs/2505.09680>.
- [75] O. Zaslavskii, *Physics Letters B* **688**, 278–280 (2010), ISSN 0370-2693, URL <http://dx.doi.org/10.1016/j.physletb.2010.04.031>.
- [76] R. K. Walia, S. G. Ghosh, and S. D. Maharaj, *The Astrophysical Journal* **939**, 77 (2022), URL <https://dx.doi.org/10.3847/1538-4357/ac9623>.
- [77] P. Kocherlakota, L. Rezzolla, H. Falcke, C. M. Fromm, M. Kramer, Y. Mizuno, A. Nathanail, H. Olivares, Z. Younsi, K. Akiyama, et al. (EHT Collaboration), *Phys. Rev. D* **103**, 104047 (2021), URL <https://link.aps.org/doi/10.1103/PhysRevD.103.104047>.
- [78] J. Neves and A. Saa, *Physics Letters B* **734**, 44–48 (2014), ISSN 0370-2693, URL <http://dx.doi.org/10.1016/j.physletb.2014.05.026>.
- [79] Frolov, Valeri P., *EPJ Web Conf.* **168**, 01001 (2018), URL <https://doi.org/10.1051/epjconf/201816801001>.
- [80] S. A. Hayward, *Phys. Rev. Lett.* **96**, 031103 (2006), URL <https://link.aps.org/doi/10.1103/PhysRevLett.96.031103>.
- [81] H. Bondi, *Nature* **186**, 535 (1960).
- [82] R. Sachs, *Proceedings of the Royal Society of London Series A* **264**, 309 (1961).
- [83] H. Bondi, M. G. J. van der Burg, and A. W. K. Metzner, *Proceedings of the Royal Society of London Series A* **269**, 21 (1962).
- [84] A. K. Divakarla and B. F. Whiting, *Physical Review D* **104** (2021), ISSN 2470-0029, URL <http://dx.doi.org/10.1103/PhysRevD.104.064001>.

### Appendix A: Riemann Tensors for the Deviation analysis

The non-zero components of  $\omega$  corresponding to Eq. (35), in the tetrad basis defined in Eq. (36), are given by:

$$\begin{aligned} \omega_1^0 &= \frac{f'(r)}{2} du & \omega_0^2 &= A(r, u) d\theta & \omega_1^2 &= B(r, u) d\theta \\ \omega_0^3 &= C(r, u) \sin \theta d\phi & \omega_1^3 &= D(r, u) \sin \theta d\phi & \omega_2^3 &= E(r, u) \cos \theta d\phi \end{aligned}$$

Where,

$$\begin{aligned} A(r, u) &= \frac{rH'(u)}{2\sqrt{f(r)(r^2 + rH(u))}} & B(r, u) &= \frac{2rf(r) + f(r)H(u) - rH'(u)}{2\sqrt{f(r)(r^2 + rH(u))}} & C(r, u) &= \frac{-rH'(u)}{2\sqrt{f(r)(r^2 - rH(u))}} \\ D(r, u) &= \frac{[2rf(r) - f(r)H(u) + rH'(u)]}{2\sqrt{f(r)(r^2 - rH(u))}} & E(r, u) &= \sqrt{\frac{r^2 - rH(u)}{r^2 + rH(u)}} \end{aligned}$$

Here our notations are as follows:  $\{u, r, \theta, \phi\} = \{0, 1, 2, 3\}$ . In that tetrad basis, non-zero Riemann tensors are:

$$\begin{aligned} R_{110}^0 &= \frac{f''(r)}{2} & R_{002}^2 &= \frac{1}{\sqrt{f(r)[r^2 + rH(u)]}} \left[ \frac{\partial A}{\partial u} - \frac{Bf'(r)}{2} \right] \\ R_{012}^2 &= \sqrt{\frac{f(r)}{r^2 + rH(u)}} \frac{\partial A}{\partial r} - R_{002}^2 & R_{112}^2 &= \sqrt{\frac{f(r)}{r^2 + rH(u)}} \frac{\partial B}{\partial r} - R_{102}^2 \\ R_{003}^3 &= \frac{1}{\sqrt{f(r)[r^2 - rH(u)]}} \left[ \frac{\partial C}{\partial u} - \frac{Df'(r)}{2} \right] & R_{013}^3 &= \sqrt{\frac{f(r)}{r^2 - rH(u)}} \frac{\partial C}{\partial r} - R_{003}^3 \\ R_{023}^3 &= \frac{C - EA}{\sqrt{r^4 - r^2 H^2(u)}} \cot \theta & R_{113}^3 &= \sqrt{\frac{f(r)}{r^2 - rH(u)}} \frac{\partial D}{\partial r} - R_{103}^3 \\ R_{123}^3 &= \frac{D - EB}{\sqrt{r^4 - r^2 H^2(u)}} \cot \theta & R_{223}^3 &= \frac{BD - E - AC}{\sqrt{r^4 - r^2 H^2(u)}} \end{aligned}$$